Mg^{2+}-electrolyte Additive Promotes High-Energy and Dendrite-free Zinc-ion Hybrid Capacitors

Pinji Wang, Xuesong Xie, Zhenyue Xing, Xianhong Chen, Guozhao Fang, Bingan Lu, Jiang Zhou,* Shuquan Liang*, and Hong Jin Fan*

P. Wang, X. Xie, Z. Xing, X. Chen, Prof. G. Fang, Prof. J. Zhou, Prof. S. Liang
School of Materials Science and Engineering, Key Laboratory of Electronic Packaging and Advanced Functional Materials of Hunan Province, Central South University, Changsha 410083 (P.R. China). E-mail: zhou_jiang@csu.edu.cn, lsq@csu.edu.cn

Prof. B. Lu
School of Physics and Electronics, Hunan University, Changsha 410082 (P.R. China)

Prof. H. J. Fan
School of Physical and Mathematical Sciences, Nanyang Technological University, Singapore 637371, Singapore. E-mail: fanhj@ntu.edu.sg

Keywords

zinc-ion hybrid capacitor, aqueous electrolyte, electrostatic shield effect, solvation-sheath structure, cation additive

Abstract: Electrolyte cation additive strategy provides a versatile route for developing high-energy and long-life aqueous zinc-ion hybrid capacitors. However, the mechanisms of energy storage and Zn anode protection are still unclear in Zn-based systems with dual-ion electrolytes. Here, we propose a dual charge storage mechanism for zinc-ion hybrid capacitors with both cations and ions adsorption/desorption and the reversible formation of $Zn_4SO_4(OH)_6{\cdot}xH_2O$ enabled by the Mg^{2+} additive in the common aqueous $ZnSO_4$ electrolyte. Theoretical calculation verifies that the self-healing electrostatic shield effect and the solvation-sheath structure regulation rendered by the Mg^{2+} additives account for the observed uniform Zn deposition and dendrite suppression. As a result, an additional energy storage capacity of about 50% than that in pure 2 M $ZnSO_4$ electrolyte and an extended cycle life with capacity retention of 98.7% after 10000 cycles are achieved. This work highlights the effectiveness of electrolyte design for dual-ion carrier storage mechanism in aqueous devices towards high energy-density and long cycle life.

Metal ion hybrid capacitors, consisting of a battery-type anode and a capacitive carbon cathode,[1, 2] have attracted increasing attention in recent years due to their merits of high power density/energy density.[3, 4] On account of the advantages of intrinsic safety, low-cost, and environmental benignity,[5] aqueous zinc-ion hybrid capacitors (ZHCs) have received significant progress especially in the cathode design, including the self-designed N-doped hierarchically porous carbon,[6] carbon hollow sphere,[7] and asymmetric hollow bowl-like carbon[8]. However, the limited capacity (~ 55 mA h g^{-1}, and 43.1 W h kg^{-1}) of commercial

porous carbon[9] associated with physical adsorption/desorption of ions in mild acidic electrolyte has refrained the progress of ZHCs.

Systematic studies have proven the existence of side reaction or by-product (zinc hydroxide sulphate hydrate) on both cathode and anode electrodes during the charge/discharge process in $ZnSO_4$-based electrolyte.[10, 11] However, the mechanism of surface redox pseudocapacitance generated by proton adsorption associated with the formation of zinc hydroxide sulphate hydrate is unascertained, and the reversibility of ZHCs lacks theoretical verification. It is known that electrolyte modification can effectively increase the capacity, depress dendrites formation and enable long cycle stability in aqueous metal Zn-based energy storage devices.[12-14] The electrolyte cation additive is an effective way compared to other methods because of its simple and economical operation.[15] Electrolyte cation additives, including Na^+,[16] Mn^{2+},[17] Co^{2+},[18] Al^{3+},[19] etc., have been widely used in aqueous zinc-ion batteries.[20] However, the storage mechanism of ZHCs is mostly based on single ion adsorption/desorption; the dual-ion carrier storage in the commonly used aqueous electrolytes is still controversial. Hence, it is imperative to conduct systematic in-depth analysis of the dual-ion storage mechanism and to develop viable strategies to significantly improve the capacity and long-cycle retention.

Herein, we report a high-energy Zn/AC hybrid capacitor using the 0.1 M $MgSO_4$ (Mg cation additive) as an active multivalent metal-ion charge carrier in the normal 2 M $ZnSO_4$ electrolyte (designated as ZnMg-0.1). The introduction of Mg^{2+} in an optimized concentration generates multiple positive effects. First, it demonstrates a self-healing electrostatic shield

effect to suppress zinc dendrites at the anode surface. Importantly, with this Mg^{2+}-mediated electrolyte, it shows reversible adsorption/desorption of both metal ions and SO_4^{2-} on the AC cathode accompanied with the invertible formation/disappearance of $Zn_4SO_4(OH)_6{\cdot}xH_2O$ (**Figure 1a**). Additional pseudocapacitance originates from the redox reaction of protons with AC surface functional groups, which is associated with the formation of $Zn_4SO_4(OH)_6{\cdot}xH_2O$ simultaneously. These effects have been verified using both a series of ex-situ characterization and molecular dynamic calculations. As a result, the ZHCs using ZnMg-0.1 electrolyte maintain a high capacity (154 mA h g^{-1} at 1 A g^{-1}) and excellent capacity retention of 98.7% even after 10000 cycles at a high current density of 5 A g^{-1}, outperforming all previously reported ZHCs.

ZHCs were fabricated to CR2016-type coin cells using commercial Zn foil and AC as the negative and positive electrode, respectively. The crystalline phase and microstructure of AC powders are given in **Figure S1** (Supporting Information). To explore the optimal electrochemical performance, a group of mixed solutions with 2 M $ZnSO_4$ and 0, 0.05, 0.1, 0.3 or 1.0 M $MgSO_4$ were applied as the electrolytes, respectively. As presented in **Figure 1b**, a high specific capacity of 154 mA h g^{-1} is achieved and remained stable for 500 cycles when the concentration of $MgSO_4$ in electrolyte is 0.1 M. Whereas the capacity is much lower and the cyclic stability is poor in pure 2 M $ZnSO_4$ without the Mg^{2+} addition (**Figure 1b**, **e**; **Figure S2**, Supporting Information). Mg^{2+} has a smaller radii (0.65 Å) compared to Zn^{2+} (0.74 Å).[21] A reversible adsorption/desorption of Mg^{2+} in the pure $MgSO_4$ electrolyte provides about 30 mA h g^{-1} capacity (**Figure S3**, Supporting Information). So it increases the capacity of ZHCs in ZnMg-0.1.[22] Noteworthily, a high concentration of $MgSO_4$ increases the viscosity of

electrolyte, and the irreversible hydrolysis of $Mg(OH)_2$ will further hinder the absorption/desorption process of Zn^{2+}.[23] EIS studies (**Figure S4** and **Table S1**, Supporting Information) also demonstrate that the AC//ZnMg-0.1//Zn cell exhibits lower resistance in ion diffusion and charge transfer.[24] The galvanostatic charge/discharge (GCD) curves under various current densities (**Figure 1c**) show decreasing slopes at both ends of the charge/discharge process, which implies the redox reaction – presumably the H^+ reaction with surface functional groups of AC that correspond to pseudocapacitance (see **Figure 1a**).[25] The Ragone plot of ZHCs with ZnMg-0.1 electrolyte in **Figure 1d** shows a high energy density of 140.25 W h kg^{-1} at the power density of 825 W kg^{-1}, and it can retain 60% of its energy density with 82.48 W h kg^{-1} at an ultrahigh power density of 16500 W kg^{-1}. These values surpass those of other recently report zinc-ion capacitors. [10, 26-30] The above results verify the effect of Mg^{2+} additive in capacity enhancement and cycling stability.

To reveal the reason to the electrochemical performance, we first investigate the AC cathode. The surface morphology and composition change to AC during charge-discharge processes were fully characterized (see **Figure 2**). The SEM (**Figure 2a**, **b**) and TEM (**Figure 2g**, **h**) images of AC cathodes suggest that the surface is covered with by-products in the fully discharged state and EDS mapping (**Figure 2e-g**) confirms that they are $Zn_4SO_4(OH)_6{\cdot}xH_2O$ particles. The $Zn_4SO_4(OH)_6{\cdot}xH_2O$ neatly wrap the surface of AC in ZnMg-0.1 and completely disappear after full charging (**Figure 2d**), suggesting that the OH^- or H^+ has participated in the reaction.[31] On the contrary, when a 2 M $ZnSO_4$ is used (**Figure 2a, c**), the flakes randomly pile up and remain with a smaller size (**Figure 2c**) in the fully charged state, suggesting the

irreversible reaction of $Zn_4SO_4(OH)_6{\cdot}xH_2O$ which is similar to common observations.[10, 32, 33] Hence, reversible ions adsorption/desorption (Equations (1) and (2)) show an electrochemical double-layer mechanism via multi-ion transportation (**Figure S5-S7**, Supporting Information).[32, 34-36] The AC has surface functional groups as confirmed by FTIR and EDS mapping (**Figure S8**, Supporting Information), which are responsible for the electrochemical H^+ adsorption/desorption (Equations (3) and (4)) during the charge-discharge processes. Change in the H^+ concentration leads to a dynamic local alkaline environment that is responsible for the formation and dissolution of $Zn_4SO_4(OH)_6{\cdot}xH_2O$ particles (Equations (5) and (6)). The *ex-situ* XRD in two cycles obviously exhibit that the characteristic peaks of $Zn_4SO_4(OH)_6{\cdot}xH_2O$ appeared when the capacitor discharged to 0.8 V and then completely disappeared after charging to 1.5 V in ZnMg-0.1 (**Figure 2i**), corresponding to the CV curves at different scan rates (**Figure S9**, **S10**, Supporting Information). The existence of irreversible peak in 2 M $ZnSO_4$ reveals the residual $Zn_4SO_4(OH)_6{\cdot}xH_2O$ even after full charging. In summary, the additional capacity delivered by the Mg^{2+}-based electrolyte is confirmed to originate from the reversible Mg^{2+} adsorption and the surface redox reaction of {AC}···H in ZHCs.

Cathode:

(1) reversible ions adsorption/desorption:

$$\{AC\} + Zn^{2+}/Mg^{2+} \leftrightarrow \{AC\}||Zn^{2+}/\{AC\}||Mg^{2+} \quad \text{(discharge/charge process)} \qquad (1)$$

$$\{AC\} + SO_4^{2-} \leftrightarrow \{AC\}||SO_4^{2-} \quad \text{(charge/discharge process)} \qquad (2)$$

(2) redox reaction:

$$\{AC\}\cdots O + H^+ + e^- \rightarrow \{AC\}\cdots O\cdots H \quad \text{(discharge process)} \qquad (3)$$

$$\{AC\}\cdots O\cdots H + OH^- - e^- \rightarrow \{AC\}\cdots O + H_2O \quad \text{(charge process)} \qquad (4)$$

(3) electrodeposition / electrolyzation:

$$Zn^{2+} + SO_4^{2-} + OH^- + H_2O \rightarrow Zn_4SO_4(OH)_6 \cdot xH_2O \quad \text{(discharge process)} \qquad (5)$$

$$Zn_4SO_4(OH)_6 \cdot xH_2O + H^+ \rightarrow Zn^{2+} + SO_4^{2-} + H_2O \quad \text{(charge process)} \qquad (6)$$

Anode:

$$Zn - e^- \rightarrow Zn^{2+}\text{(discharge process)} \,/\, Zn^{2+} + e^- \rightarrow Zn\text{(charge process)} \qquad (7)$$

Effect of the Mg^{2+} additive to the stability of Zn anode has also been systematically evaluated. As observed in **Figure 3a**, the Zn//2 M $ZnSO_4$//Zn symmetrical coin cell only sustains less than 424 h prior to a short circuit. For ZnMg-0.1, it can maintain more than 600 h with highly stable voltage-time profiles and smaller voltage hysteresis (44.6 mV *vs.* Zn^{2+}/Zn) than that of 2 M $ZnSO_4$ (56.5 mV). Even at a higher current density of 4 mA cm^{-2}, the Zn//ZnMg-0.1//Zn symmetrical cell can also stabilize for 800 h with the overpotential of less than 0.1 V (**Figure S11**, Supporting Information). Similarly, the values of Coulombic efficiency (CE) during long-term cycling in Zn/Cu cell also proved the efficiency of Zn plating/stripping in ZnMg-0.1 (**Figure S12**, Supporting Information). The surface morphological changes of Zn anode after continuous plating and stripping were also confirmed by electron probe microanalysis (EPMA), ultra-depth three-dimensional microscope (UTM) optical analyses and SEM. Compared to the Zn electrode in 2 M $ZnSO_4$ (**Figure S13**, Supporting Information), **Figure 3b** shows a homogeneous distribution and higher concentration (up to 92.29% *vs.* 71.29% in pure $ZnSO_4$ electrolyte) of the Zn element. And the O element is 0.49% *vs.* 3.12%,

respectively (**Figure 3c**). Accordingly, for large-scale observation, UTM optical analyses of Zn anode in 2 M $ZnSO_4$ after 20 cycles reveal an accumulated surface **(Figure 3d-f)**. In contrast, it is clear to see that the surface of Zn anode in ZnMg-0.1 is smooth and assimilated with Zn substrate (**Figure S14**, Supporting Information). XRD patterns (**Figure S15**, Supporting Information) imply the corrosion of Zn metal and formation of $Zn_4SO_4(OH)_6{\cdot}xH_2O$ during the plating/stripping process in 2 M $ZnSO_4$. The loose $Zn_4SO_4(OH)_6{\cdot}xH_2O$ layer generated between Zn metal and electrolyte may prevent the ions and electronic transport at the interface, which further blocks Zn stripping and plating [37].

SEM observations (**Figure 3g**, **h**) are conducted to reveal the intrinsic growth mode of Zn after 20 cycles of plating and stripping. Flake-shaped Zn dendrites and cracks are generated on Zn foil, which is a typical feature of Zn anode in mild acidic 2 M $ZnSO_4$ electrolyte due to the side reaction and archetypical tip-growth theory of Zn ions deposition.[38, 39] In sharp contrast, with the Mg^{2+} additive, the dendritic flakes have been transformed into regular hexagonal prisms and they grow compactly within the surface. Unlike the corrosion pits on the Zn surface formed by side reaction in 2 M $ZnSO_4$, the SEM image of Zn in ZnMg-0.1 shows a smooth garment, which is similar to the untreated Zn (**Figure S16**, Supporting Information). These two different behaviors illustrate the decisive role of the Mg^{2+} additive in guiding the Zn deposition behavior, leading to a uniform plating layer without evident Zn dendrites, as discussed in detail below.

The concentration of $MgSO_4$ additive is optimized from a series of control experiments. SEM images of AC cathode discharged to 0.2 V and Zn anode after 20 stripping/plating cycles

(**Figure S17**, Supporting Information) with increasing concentration of $MgSO_4$ show the different results very clearly. The $MgSO_4$ additives with low concentrations (<0.1 M) have less prominent effect in suppressing Zn dendrites and side reactions on AC cathode. When the concentration is higher than 0.1 M, the excessive Mg^{2+} additive might lead to an increase in the acidity of the electrolyte due to the hydrolysis reaction of $MgSO_4$. According to the *in-situ* pH analysis (**Figure S18**, Supporting Information), the pH value of the ZnMg-0.1 electrolyte has a smaller fluctuation than that of the pristine $ZnSO_4$ electrolyte after certain cycles. While in ZnMg-1.0, the pH value fluctuates drastically and exhibits a lower average value, indicating a severe side reaction. During the shelving process (**Figure S19**, Supporting Information), the pH value remains nearly constant in ZnMg-1.0 while it increases for the 2 M ZnSO4 electrolyte, which might be associated with the hydrogen evolution reaction and irreversible precipitation reaction of $Zn_4SO_4(OH)_6{\cdot}xH_2O$ occurred on the Zn anode.

To obtain better insights into the mechanism of the Mg^{2+} additive in electrolyte, the interaction between the electrolyte and Zn anode was studied by the Nernst equation and DFT calculation. Calculation using the Nernst equation (Supporting Information) show that, Mg^{2+} (-2.402 V, 0.1 M) has a lower effective reduction potential compared with Zn^{2+} (-0.751 V, 2 M) (**Figure 4a**). As a result, Mg^{2+} will not be reduced to Mg metal on the Zn anode surface; and indeed no Mg can be detected according to the EDS analysis (**Figure S20**, Supporting Information).[40, 41] The DFT results of adsorption energy on Zn surface with different electrolyte components in **Figure 4b** exhibit a lower E_{ads} of $MgSO_4$ (-1.953 eV) than that of $ZnSO_4$ (-0.472 eV), indicating that Mg^{2+} is preferentially adsorbed on Zn anode. **Figure 4c**

schematically explains the effect of Mg^{2+} additive on Zn^{2+} desolvation and deposition. Due to the incomplete desolvation of $Zn(H_2O)_6^{2+}$, bare Zn suffers from the interface side reactions and hydrogen evolution of water molecules (**Figure S21**, Supporting Information).[42] The formation of Zn dendrites during cycling can be described as a "tip effect",[43] that the elevated tip electric field aggravates the growth of Zn dendrite. The adsorbed Mg^{2+} with a lower effective reduction potential will accumulate around the Zn dendrites to form an electrostatic shield. Thus, Zn^{2+} ions will not continue to pile on the dendrite but instead deposit to adjacent flat surfaces, leading to a smooth deposition layer on the Zn anode.[44]

To verify the hypothesis of Zn deposition process, the radial distribution functions of Mg-O (H_2O) and Zn-O (H_2O) pairs are calculated by MD simulation. The obtained trajectories (**Figure 5a**) show that the peaks of Zn-O pair are located at 3.14 Å for both electrolyte systems, while a sharp peak of Mg-O pair is identified at 2.84 Å. It implies that Mg^{2+} has a close binding interaction with water molecules and impairs H_2O from the Zn^{2+} solvation sheath. In addition, due to the $MgSO_4$, the hydration water can be dominated by local electric field of the ions, leading to reduction of water activity by inhibiting the vibration.[45] The solvation-sheath structure of electrolytes in ZHCs is further studied using Raman spectroscopy (**Figure 5b**; **Figure S22**, Supporting Information). The peaks of M-OSO_3^{2-} (M=Zn^{2+}, Mg^{2+}, ca. 235 cm^{-1}) and v_4-SO_4^{2-} (610 cm^{-1}) exhibit suppressed vibration in ZnMg-0.1, corresponding to a weakened chemical bonding with cations (**Table S2**). Based on the classic Eigen–Tamm mechanism, the two types of ion-associations (SSIP, $Zn^{2+}(H_2O)_6SO_4^{2-}$; CIP, $Zn^{2+}(H_2O)_5OSO_3^{2-}$) show different Zn^{2+}-solvation-shell structures (**Figure 5e**). The percentages of two ion-pair species are 78.96%

in SSIP and 21.04% in CIP for the ZnMg-0.1 electrolyte (**Table S3**), indicating a weaker interaction between Zn^{2+} and SO_4^{2-} that is conducive to preventing the SO_4^{2-} from participating in side reactions on Zn surface. Moreover, the v_1-SO_4^{2-} band shifts to a lower frequency (ca. 985 cm^{-1}), also suggesting a more distant Zn^{2+}-SO_4^{2-} ion association.[46] The band of O-H vibration (HOH-OH_2 stretch, 3270 cm^{-1}; HOH-OSO_3^{2-} dominate, 3450 cm^{-1}) shifts to high frequency in ZnMg-0.1, which is consistent to the decrease of the free water molecule ratio.[47, 48] To unravel the solvation-shell structure of Zn^{2+} in different electrolytes, molecular dynamics simulations were performed in **Figure 5c**, **d** and **Figure S23** (Supporting Information). In 2 M $ZnSO_4$, Zn^{2+} is solvated by H_2O and SO_4^{2-} ($Zn(H_2O)_6^{2+}SO_4^{2-}$), while in ZnMg-0.1, Zn^{2+} and Mg^{2+} share the surrounding solvated H_2O and SO_4^{2-} together ($Zn^{2+}Mg^{2+}(H_2O)_6SO_4^{2-}$). This is in accordance with Raman results and may account for the suppressed side reaction and uniform deposition of Zn.

In summary, based on self-healing electrostatic shield mechanism and dual-ion carrier storage mechanism, we have achieved new ZHC devices with high energy density and long-cycle-life by optimizing the aqueous sulfate electrolyte. The mechanism differs from the conventional physical adsorption of SO_4^{2-} on AC. The adsorption of Mg^{2+} and the surface redox pseudocapacitance provided by reversible proton adsorption associated with the formation of $Zn_4SO_4(OH)_6{\cdot}xH_2O$ contribute to the additional capacity. On the Zn anode side, the Mg^{2+} additive demonstrates the positive effect in inhibiting the hydrogen evolution, enabling a uniform nucleation and deposition of Zn and suppressing the growth of Zn dendrites. The electrolyte solvation structure regulation is confirmed by theoretical calculation. Our study has

demonstrated that electrolyte cation additive is an effective approach for electrolyte optimization towards building a safe and stable Zn-based energy storage device.

Supporting Information

Supporting Information is available from the Wiley Online Library or from the author.

Acknowledgements

P. W. and X. X. contributed equally to this work. This work was supported by National Natural Science Foundation of China (Grant Nos. 51932011, 51972346), the Program of Youth Talent Support for Hunan Province (2020RC3011), Innovation-Driven Project of Central South University (No. 2020CX024), and the Fundamental Research Funds for the Central Universities of Central South University (No. 202321024). H.J.F acknowledges the financial support from Ministry of Education by Tier 1 grant (RG157/19).

Conflict of Interest

The authors declare no conflict of interest.

References

[1] P. Simon, Y. Gogotsi, *Nat. Mater*. **2020**, *19*, 1151.

[2] Y. Wang, Y. Song, Y. Xia, *Chem. Soc. Rev*. **2016**, *45*, 5925.

[3] L. Dong, W. Yang, W. Yang, Y. Li, W. Wu, G. Wang, *J. Mater. Chem. A*. **2019**, *7*, 13810.

[4] S. Wang, Q. Wang, W. Zeng, M. Wang, L. Ruan, Y. Ma, *Nano-Micro Lett*. **2019**, *11*, 70.

[5] X. Jia, C. Liu, Z. G. Neale, J. Yang, G. Cao, *Chem. Rev*. **2020**, *120*, 7795.

[6] H. Zhang, Q. Liu, Y. Fang, C. Teng, X. Liu, P. Fang, Y. Tong, X. Lu, *Adv. Mater*. **2019**, *31*, e1904948.

[7] P. Liu, W. Liu, Y. Huang, P. Li, J. Yan, K. Liu, *Energy Storage Mater*. **2020**, *25*, 858.

[8] R. Fei, H. Wang, Q. Wang, R. Qiu, S. Tang, R. Wang, B. He, Y. Gong, H. Fan, *Adv. Energy Mater*. **2020**, *10*, 2002741.

[9] Y. Lu, Z. Li, Z. Bai, H. Mi, C. Ji, H. Pang, C. Yu, J. Qiu, *Nano Energy* **2019**, *66*, 104132.

[10] L. Dong, X. Ma, Y. Li, L. Zhao, W. Liu, J. Cheng, C. Xu, B. Li, Q.-H. Yang, F. Kang, *Energy Storage Mater*. **2018**, *13*, 96.

[11] Z. Huang, T. Wang, H. Song, X. Li, G. Liang, D. Wang, Q. Yang, Z. Chen, L. Ma, Z. Liu, B. Gao, J. Fan, C. Zhi, *Angew Chem. Int. Ed*. **2020**, *60*, 1011.

[12] T. Zhang, Y. Tang, S. Guo, X. Cao, A. Pan, G. Fang, J. Zhou, S. Liang, *Energy Environ. Sci.* **2020**, *13*, 4625.

[13] J. Zeng, L. Dong, L. Sun, W. Wang, Y. Zhou, L. Wei, X. Guo, *Nano-Micro Lett*. **2020**, *13*, 19.

[14] L. Cao, D. Li, E. Hu, J. Xu, T. Deng, L. Ma, Y. Wang, X. Yang, C. Wang. *J. Am. Chem. Soc*. **2020**, *142*, 21404.

[15] J. Hao, J. Long, B. Li, X. Li, S. Zhang, F. Yang, X. Zeng, Z. Yang, W. K. Pang, Z. Guo, *Adv. Funct. Mater*. **2019**, *29*, 1903605.

[16] F. Wan, L. Zhang, X. Dai, X. Wang, Z. Niu, J. Chen, *Nat. Commun*. **2018**, *9*, 1656.

[17] H. Pan, Y. Shao, P. Yan, Y. Cheng, K. S. Han, Z. Nie, C. Wang, J. Yang, X. Li, P. Bhattacharya, K. T. Mueller, J. Liu, *Nat. Energy.* **2016**, *1*, 16039.

[18] L. Ma, S. Chen, H. Li, Z. Ruan, Z. Tang, Z. Liu, Z. Wang, Y. Huang, Z. Pei, J. A. Zapien, C. Zhi, *Energy Environ. Sci*. **2018**, *11*, 2521.

[19] N. Li, G. Li, C. Li, H. Yang, G. Qin, X. Sun, F. Li, H. M. Cheng, *ACS Appl. Mater. Inter*. **2020**, *12*, 13790.

[20] S. Guo, L. Qin, T. Zhang, M. Zhou, J. Zhou, G. Fang, S. Liang, *Energy Storage Mater*. **2021**, *34*, 545.

[21] D. Chao,W. Zhou, F. Xie, C. Ye, H. Li, M. Jaroniec, S. Qiao, *Sci. Adv*. **2020**, *6*, eaba4098.

[22] H. Zhang, K. Ye, K. Zhu, R. Cang, X. Wang, G. Wang, D. Cao, *ACS Sustain. Chem. Eng*. **2017**, *5*, 6727.

[23] M.-H. Grosjean, L. Roué, *J. Alloy. Compd*. **2006**, *416*, 296.

[24] K. A. Owusu, X. Pan, R. Yu, L. Qu, Z. Liu, Z. Wang, M. Tahir, W. A. Haider, L. Zhou, L. Mai, *Mater. Today Energy*. **2020**, *18*, 100529.

[25] Y. Shao, M. F. El-Kady, J. Sun, Y. Li, Q. Zhang, M. Zhu, H. Wang, B. Dunn, R. B. Kaner, *Chem. Rev*. **2018**, *118*, 9233.

[26] J. Shi, S. Wang, Q. Wang, X. Chen, X. Du, M. Wang, Y. Zhao, C. Dong, L. Ruan, W. Zeng, *J. Power Sources* **2020**, *446*, 227345.

[27] Y. Zheng, W. Zhao, D. Jia, Y. Liu, L. Cui, D. Wei, R. Zheng, J. Liu, *Chem. Eng. J*. **2020**, *387*, 124161.

[28] B. D. Boruah, B. Wen, S. Nagane, X. Zhang, S. D. Stranks, A. Boies, M. D. Volder, *ACS Energy Lett*. **2020**, *5*, 3132.

[29] D. Chao, C. Zhu, M. Song, P. Liang, X. Zhang, N. H. Tiep, H. Zhao, J. Wang, R. Wang, H. Zhang, H. Fan, *Adv. Mater*. **2018**, *30*, e1803181.

[30] J. Yin, W. Zhang, W. Wang, N. A. Alhebshi, N. Salah, H. N. Alshareef, *Adv. Energy Mater*. **2020**, *10*, 2001705.

[31] S. J. Kim, D. Wu, N. Sadique, C. D. Quilty, L. Wu, A. C. Marschilok, K. J. Takeuchi, E. S. Takeuchi, Y. Zhu, *Small*. **2020**, *16*, e2005406.

[32] X. Deng, J. Li, Z. Shan, J. Sha, L. Ma, N. Zhao, *J. Mater. Chem. A*. **2020**, *8*, 11617.

[33] L. Li, T. K. A. Hoang, J. Zhi, M. Han, S. Li, P. Chen, *ACS Appl. Mater. Inter*. **2020**, *12*, 12834.

[34] Y. Jin, H. Ao, K. Qi, X. Zhang, M. Liu, T. Zhou, S. Wang, G. Xia, Y. Zhu, *Mater. Today Energy*. **2021**, *19*, 100598.

[35] Y. Tian, R. Amal, D.-W. Wang, *Front. Energy Res*. **2016**, *4*, 34.

[36] Q. Liu, H. Zhang, J. Xie, X. Liu, X. Lu, *Carbon Energy*. **2020**, *2*, 521.

[37] J. Hao, B. Li, X. Li, X. Zeng, S. Zhang, F. Yang, S. Liu, D. Li, C. Wu, Z. Guo, *Adv. Mater*. **2020**, *32*, e2003021.

[38] J. Cui, X. Liu, Y. Xie, K. Wu, Y. Wang, Y. Liu, J. Zhang, J. Yi, Y. Xia, *Mater. Today Energy* **2020**, *18*, 100563.

[39] Y. Tang, C. Liu, H. Zhu, X. Xie, J. Gao, C. Deng, M. Han, S. Liang, J. Zhou, *Energy Storage Mater*. **2020**, *27*, 109.

[40] F. Ding, W. Xu, G. L. Graff, J. Zhang, M. L. Sushko, X. Chen, Y. Shao, M. H. Engelhard, Z. Nie, J. Xiao, X. Liu, P. V. Sushko, J. Liu, J. Zhang, *J Am. Chem. Soc*. **2013**, *135*, 4450.

[41] X. Chen, X. Shen, T.-Z. Hou, R. Zhang, H.-J. Peng, Q. Zhang, *Chem*. **2020**, *6*, 2242.

[42] X. Xie, S. Liang, J. Gao, S. Guo, J. Guo, C. Wang, G. Xu, X. Wu, G. Chen, J. Zhou, *Energy Environ. Sci*. **2020**, *13*, 503.

[43] X.-B. Cheng, T.-Z. Hou, R. Zhang, H.-J. Peng, C.-Z. Zhao, J.-Q. Huang, Q. Zhang, *Adv. Mater*. **2016**, *28*, 2888.

[44] Z. Ye, Z. Cao, M. O. Lam Chee, P. Dong, P. M. Ajayan, J. Shen, M. Ye, *Energy Storage Mater*. **2020**, *32*, 290.

[45] F. Novelli, L. R. Pestana, K. C. Bennett, F. Sebastiani, E. M. Adams, N. Stavrias, T. Ockelmann, A. Colchero, C. Hoberg, G. Schwaab, T. Head-Gordon, M. Havenith, *J. Phys. Chem. B*. **2020**, *124*, 4989.

[46] W. W. Rudolph, M. H. Brooker, P. Tremaine, *Für Phy. Chem*. **1999**, *209*, 181.

[47] H. Yang, Y. Qiao, Z. Chang, H. Deng, P. He, H. Zhou, *Adv. Mater*. **2020**, *32*, e2004240.

[48] H. Yang, Z. Chang, Y. Qiao, H. Deng, X. Mu, P. He, H. Zhou, *Angew Chem. Int. Ed.* **2020**, *59*, 9377.

Figures and Captions

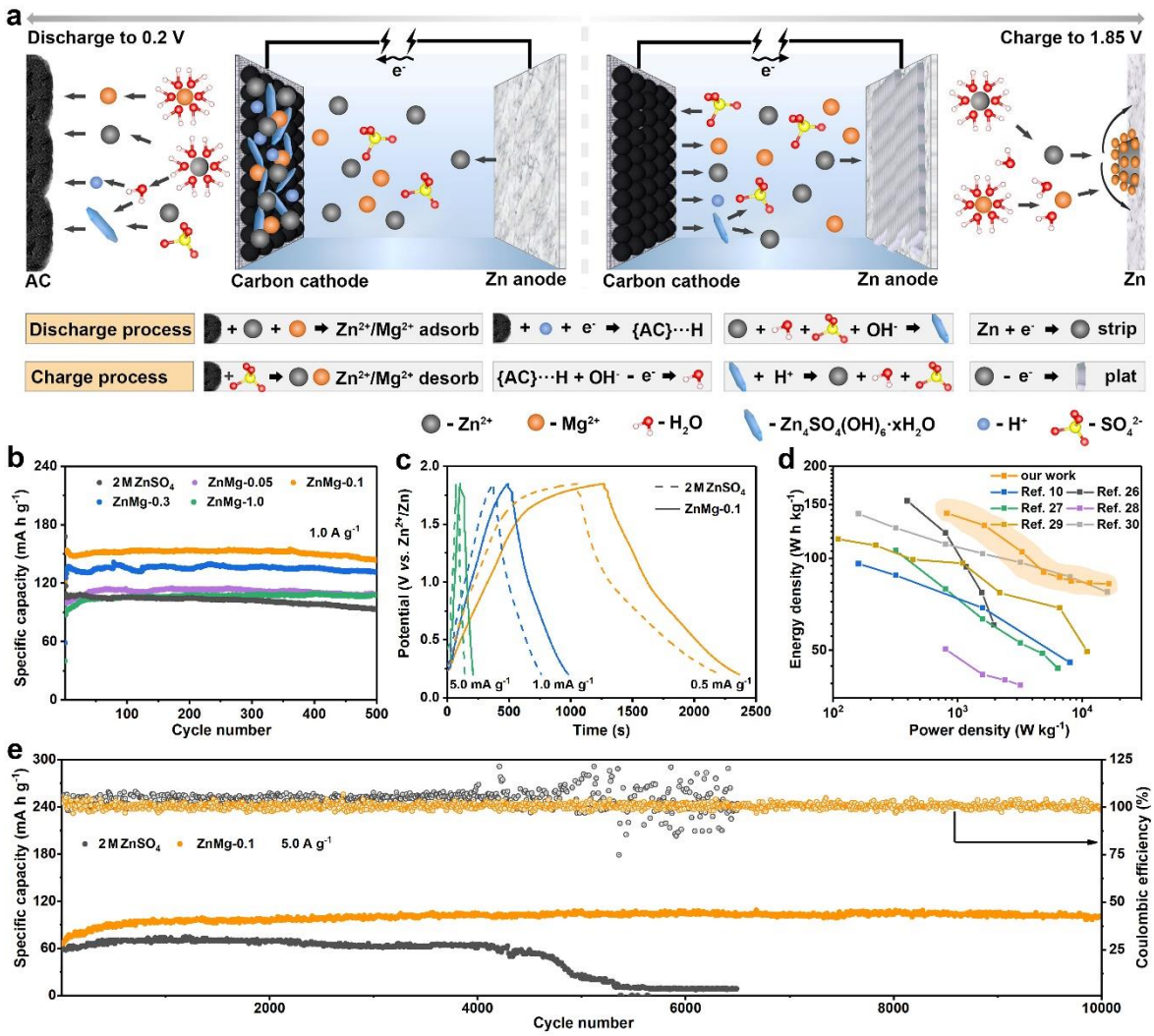

Figure 1. Working mechanism and electrochemical behaviors of ZHCs in optimized dual-cation aqueous electrolyte. a) Schematic of AC//ZnMg-0.1//Zn energy storage devices. b) Comparison of the cycling performance with different concentrations of $MgSO_4$ additive in the electrolyte. c) GCD curves at different current densities of 0.5–5.0 A g^{-1} in $ZnSO_4$ and ZnMg-0.1 electrolytes. d) Energy and power density plots of the ZHC device with ZnMg-0.1 electrolyte in comparison to other reported Zn-ion capacitors. e) Long-term cycling performance at 5.0 A g^{-1} in pure $ZnSO_4$ and ZnMg-0.1 electrolytes.

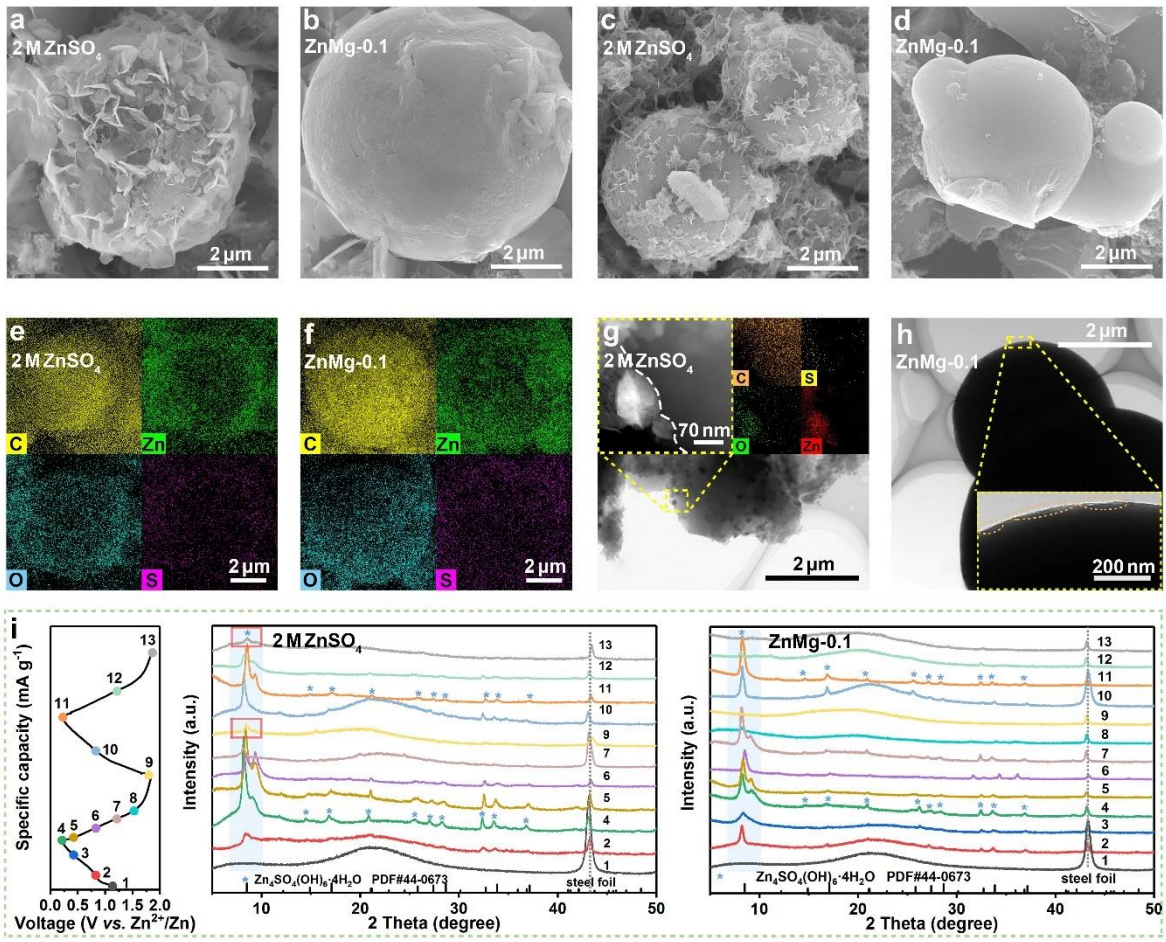

Figure 2. Effect of Mg^{2+} additive to the AC cathode. SEM images of AC electrodes in 2 M $ZnSO_4$ and ZnMg-0.1 electrolytes: a, b) discharge state and c, d) charge state. e, f) EDS mapping images of AC cathodes in the fully discharged state with the two electrolytes. g) TEM and STEM-EDS mapping images in 2 M $ZnSO_4$ and h) TEM images in ZnMg-0.1 of AC electrodes discharge to 0.2 V. i) Galvanostatic charge-discharge curve and *ex-situ* XRD patterns of AC electrodes in two electrolytes during first two cycles at the current density of 0.2 A g^{-1}.

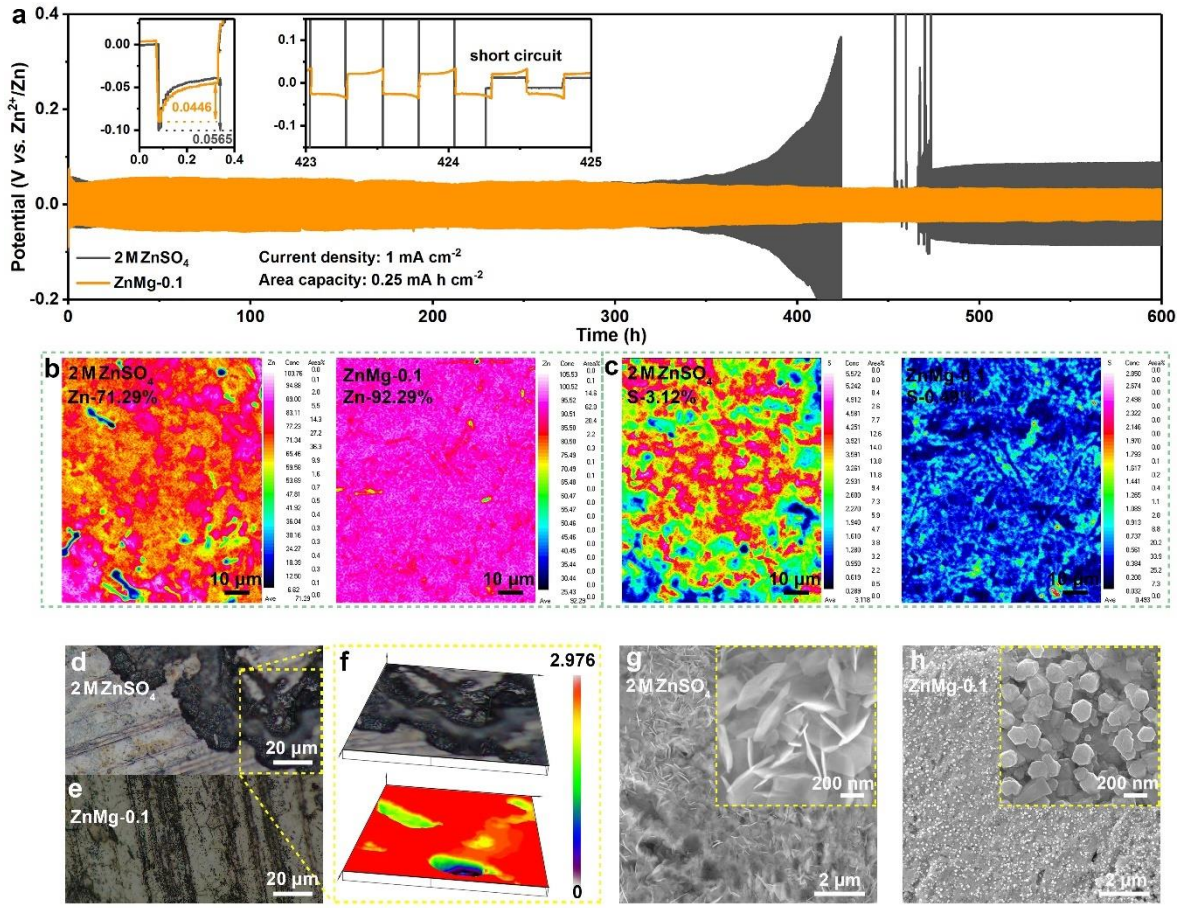

Figure 3. Effect of Mg^{2+} additive to the Zn anode. a) Long-term galvanostatic cycling performance of symmetrical cells in 2 M $ZnSO_4$ and ZnMg-0.1 electrolytes. b, c) EPMA mapping images of Zn foil electrodes after 20 cycles in 2 M $ZnSO_4$ and ZnMg-0.1. d-f) The UTM optical images of Zn electrodes in the two electrolytes after 20 cycles and enlarged views. g, h) SEM images of Zn electrodes in the two electrolytes in the fully charged state after 20 cycles.

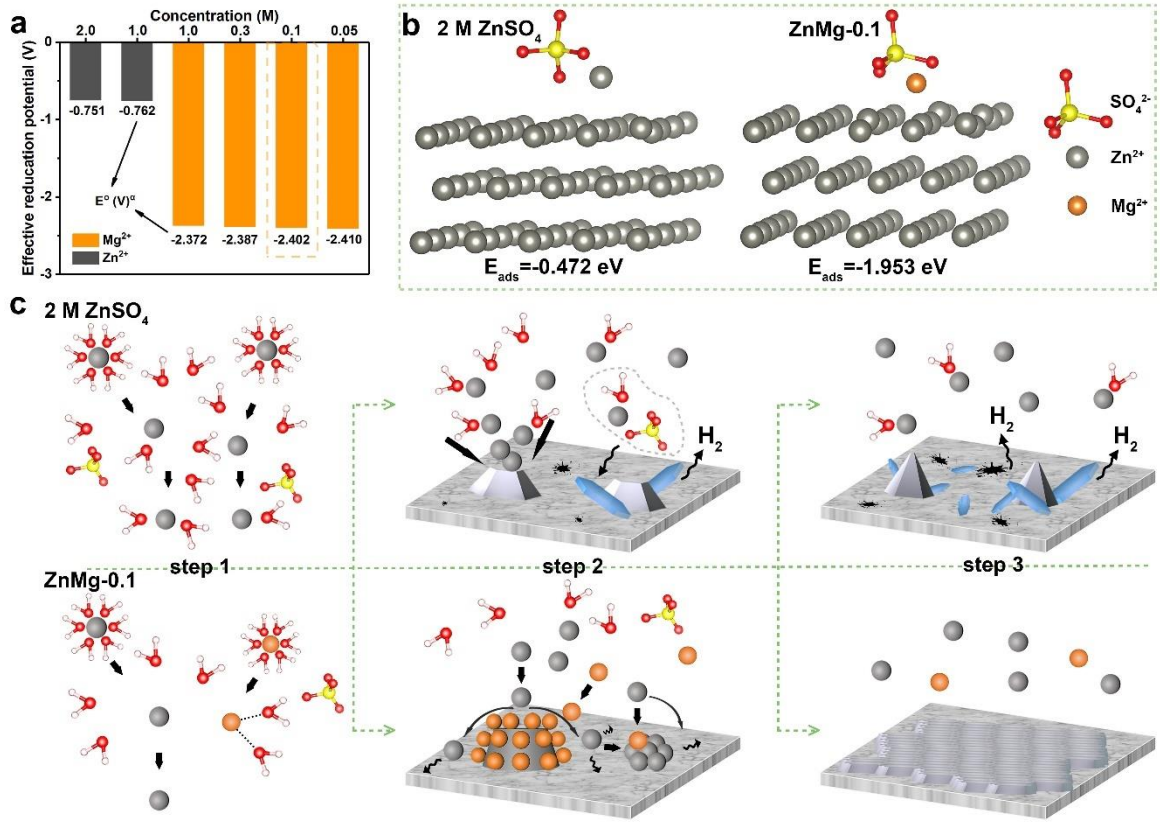

Figure 4. The interaction between the electrolyte and Zn anode in ZHCs. a) Effective reduction potentials of Zn^{2+} and Mg^{2+} at different concentrations. b) Adsorption of electrolyte ions on a Zn surface and corresponding adsorption energy (E_{ads}). c) Schematics of Zn deposition process in the 2 M $ZnSO_4$ (top row) and ZnMg-0.1 (bottom row) electrolyte.

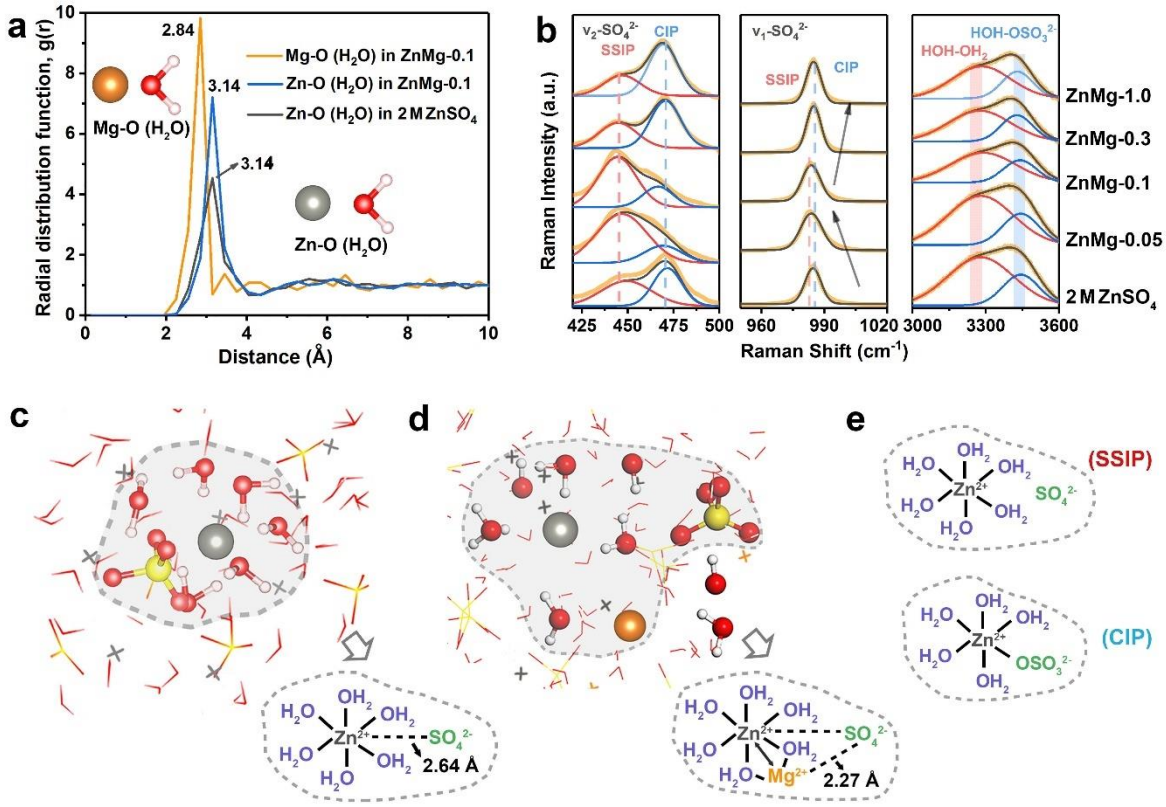

Figure 5. a) Radial distribution functions of Mg-O and Zn-O pairs calculated from the MD simulations. b) Raman spectra of different concentrations of $MgSO_4$ additive in 2 M $ZnSO_4$. c, d) Representative Zn^{2+}-solvation structures in 2 M $ZnSO_4$ (c) and ZnMg-0.1 (d) from MD simulations. e) Ion-associations of SSIP and CIP.

TOC Entry

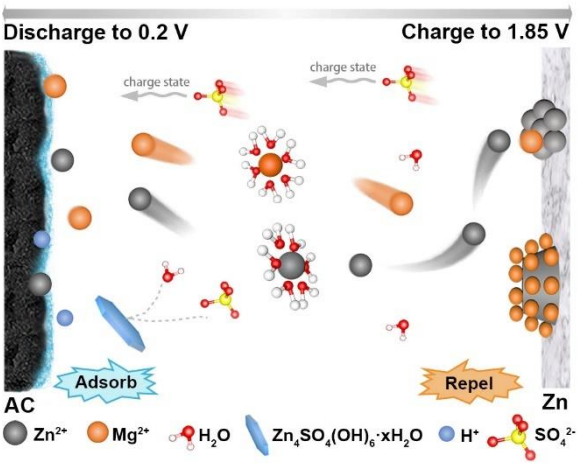

We report a high-capacity Zn-based hybrid capacitor using the 0.1 M $MgSO_4$ (Mg cation additive) as an active multivalent metal-ion charge carrier in 2 M $ZnSO_4$ electrolyte. The Mg^{2+} additive contributes additional capacity, inhibits side reactions, and suppresses Zn dendrites by facilitating a uniform Zn nucleation and deposition.

Supporting Information for

Mg^{2+}-electrolyte Additive Promotes High-Energy and Dendrite-free Zinc-ion Hybrid Capacitors

Pinji Wang, Xuesong Xie, Zhenyue Xing, Xianhong Chen, Guozhao Fang, Bingan Lu, Jiang Zhou,* Shuquan Liang*, and Hong Jin Fan*

P. Wang, X. Xie, Z. Xing, X. Chen, Prof. G. Fang, Prof. J. Zhou, Prof. S. Liang
School of Materials Science and Engineering, Key Laboratory of Electronic Packaging and Advanced Functional Materials of Hunan Province, Central South University, Changsha 410083 (P.R. China). E-mail: zhou_jiang@csu.edu.cn, lsq@csu.edu.cn

Prof. B. Lu
School of Physics and Electronics, Hunan University, Changsha 410082 (P.R. China)

Prof. H. J. Fan
School of Physical and Mathematical Sciences, Nanyang Technological University, Singapore 637371, Singapore. E-mail: fanhj@ntu.edu.sg

Experimental section

Electrochemical measurements

Activated carbon (AC) raw material was produced by Jinan Shengquan Group Share Holding Co., Ltd. in China. The cathode electrode was composed of AC, conductive carbon black and polyvinylidene fluoride at a mass ratio of 8:1:1 in N-methyl pyrrolidone solvent. The mixture was coated on steel mesh and then dried at 80℃ for 12 hours in a vacuum oven. Zn/AC energy storage devices were coupled with the electrolyte of 2 M $ZnSO_4$ with/without 0.1 M $MgSO_4$ as an additive in H_2O, separator of glass fiber and the anode of Zn foil into CR2016 coin cells. Galvanostatic charge/discharge cycling measurements were carried out on the LAND battery test instrument (LAND CT2001, China) at different current densities at room temperature. Cyclic voltammetry (CV) profiles were performed on an electrochemical station (CHI660E, China) at different scan rates with a voltage range of 0.2-1.85 V, in which electrochemical impedance spectrometry (EIS) was also tested within the frequency range from 10^{-2} to 10^5 Hz.

Material characterizations

X-ray diffraction (XRD) measurements were carried out on the Rigaku Mini Flex 600 diffractometer with Cu Kα-radiation (λ=1.5418 Å). Brumaire-Emmett-Teller (BET) and Barrett–Joyner–Halenda (BJH) analyzers were determined by micromeritics ASAP 2460 to test specific surface area and pore structure of raw AC granules. The scanning electron microscope (SEM, MIRA3 TESCAN, 10 kV) and transmission electron microscope (TEM, Titan G2 60-300) were employed to scan the microcosmic surface morphology and dendritic crystal. The ultra-depth three-dimensional microscope was performed on the Keyence VHX-5000 instrument. Electron probe microanalysis was conducted by JXA-8230 facilities with wavelength-dispersive X-ray spectroscopy (WDS) characterization. The Raman spectra were employed by HR Evolution (HORIBA) confocal Raman spectrometer to obtain the Raman signal of the mixture electrolyte. The excitation laser at 632.8 nm/0.5 m W was focused with 600 gr mm^{-1} optical grating through a 50×long-working-distance lens (N.A.=0.5, WD=10.6 mm). The Raman spectrum acquisition time was 30 s with three cycles. To reduce the background from the fluorescence, the pinhole was set at 50 μm.

Computational methods

The first-principles[1, 2] were employed to perform all Spin-polarization density functional theory (DFT) calculations within the generalized gradient approximation (GGA) using the Perdew-Burke-Ernzerhof (PBE)[3] formulation. Projector-augmented-wave (PAW)[4, 5] type pseudopotentials, as implemented in the VASP source code package, are used to describe the ionic cores and the electronic structure is described using a plane-wave basis set with a kinetic

energy cutoff of 400eV. Partial occupancies of the Kohn−Sham orbitals were allowed using the Gaussian smearing method and a width of 0.05 eV. The electronic energy was considered self-consistent when the energy change was smaller than 10^{-6} eV. Geometry optimization was deemed to be convergent when the energy change was smaller than 0.05 eV $Å^{-1}$. Finally, the adsorption energies (Eads) were calculated as:$E_{ads} = E_{ad/sub} - E_{ad} - E_{sub}$, where $E_{ad/sub}$, E_{ad}, and E_{sub} are the total energies of the optimized adsorbate/substrate system, the adsorbate in the gas phase, and the clean substrate, respectively.

Molecular dynamics (MD) simulations were performed to investigate the ion separation mechanism.[6] The condensed-phased-optimized molecular potential for atomistic simulation studies force field has been employed to optimize. In the modeling, the structure was initially constructed with anions and cations to reach a better property, and the simulation structure is established. In addition, the complex is also applied hexagonal symmetry to construct our model, and the cell size is 32.11×32.11×32.11 Å.[7] To obtain a global minimum energy configuration, geometry optimization is first performed using the method of GGA-PBE.[8] The unit cells are then allowed to equilibrate over NPT simulations (isothermal-isobaric ensemble) at a room temperature of 300 K and an atmospheric pressure of 101 KPa for 20 ns with a time step of 1 fs. The molecular equilibration systems can be obtained after a geometry optimization.

Supplementary Figures

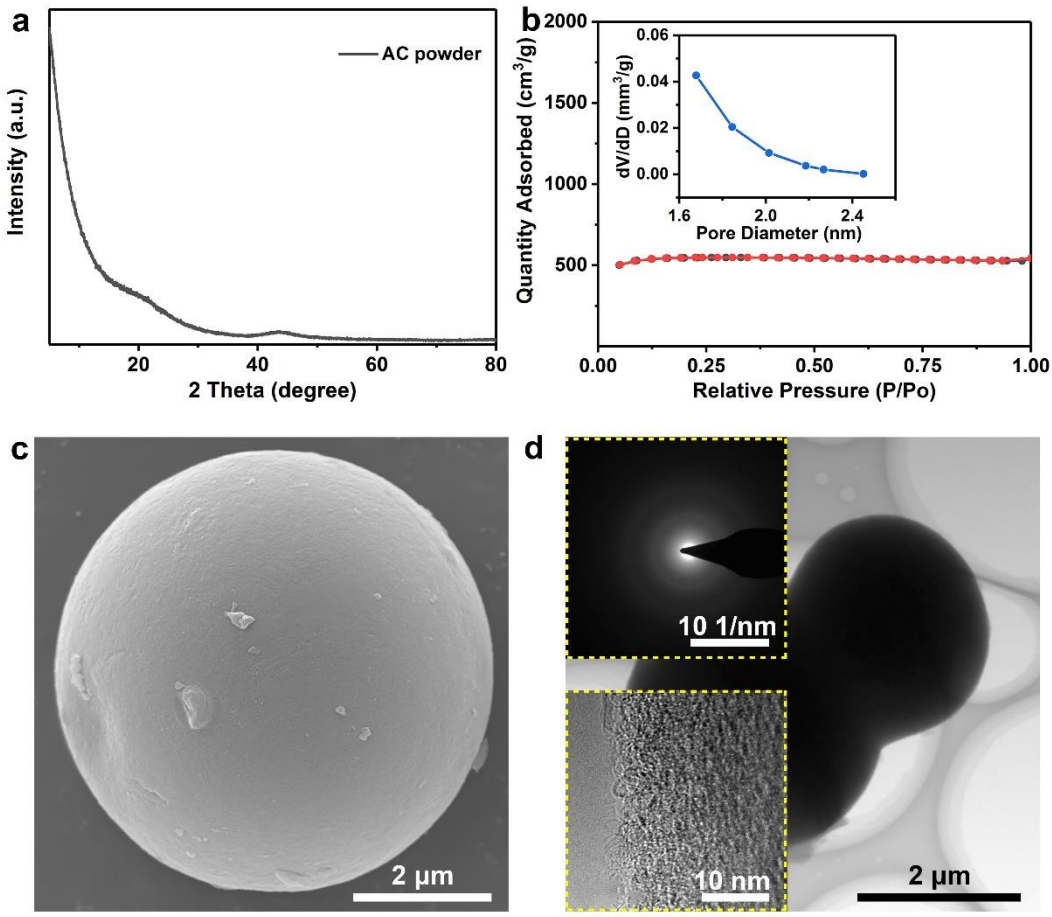

Figure S1. XRD, BET analysis and morphologies of AC raw materials. a) XRD pattern. b) BET and pore size distribution. c) SEM image. d) TEM image, HRTEM image and SAED pattern.

The XRD pattern of AC dispirits two typical diffraction peaks of carbon (**Figure S1a**). Based on BET and BJH analysis in **Figure S1b**, the specific surface area and pore volumes are 1534.5 $m^2\ g^{-1}$ and 0.77 $cm^3\ g^{-1}$. The carbon sphere structure and disordered pore are proved by SEM and TEM (**Figure S1c, d**). It can be clear observed that amorphous porous carbon structure occupied the whole vision.

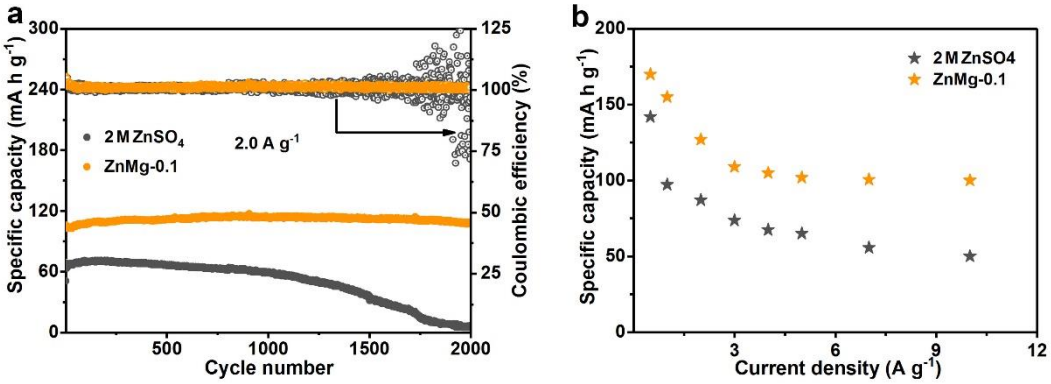

Figure S2. a) Cycling performances of ZIHCs in 2 M $ZnSO_4$ and ZnMg-0.1 at current densities with 2 A g^{-1}. b) Rate capacity of ZIHCs in 2 M $ZnSO_4$ and ZnMg-0.1.

As measured in **Figure S2**, the cycling performance and rate capability of ZHCs in ZnMg-0.1 are much better than that in pure 2 M $ZnSO_4$. **Figure S2a** shows the at the current density of 2.0 A g^{-1}, high specific capacity with nearly 100% CE after 2000 cycles is achieved in 2 M ZnMg-0.1, whereas, the ZHCs in 2 M $ZnSO_4$ only run less than 2000 cycles and then fall down. In **Figure S2b**, the cycling performances of ZHCs in ZnMg-0.1 display about 1.5 times capacity improvement compared to 2 M $ZnSO_4$ at different current densities.

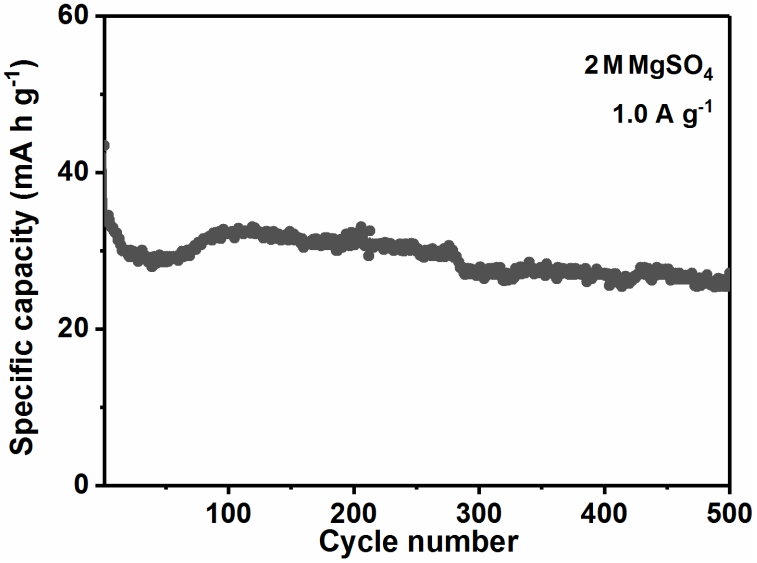

Figure S3. Cycling performance of AC//2 M $MgSO_4$//Zn capacitor with the current densities of 1.0 A g^{-1}

With only $MgSO_4$ solution, the reversible adsorption of Mg^{2+} indicates the external capacity contribution about 30 mA h g^{-1} at the current density of 1.0 A g^{-1}.

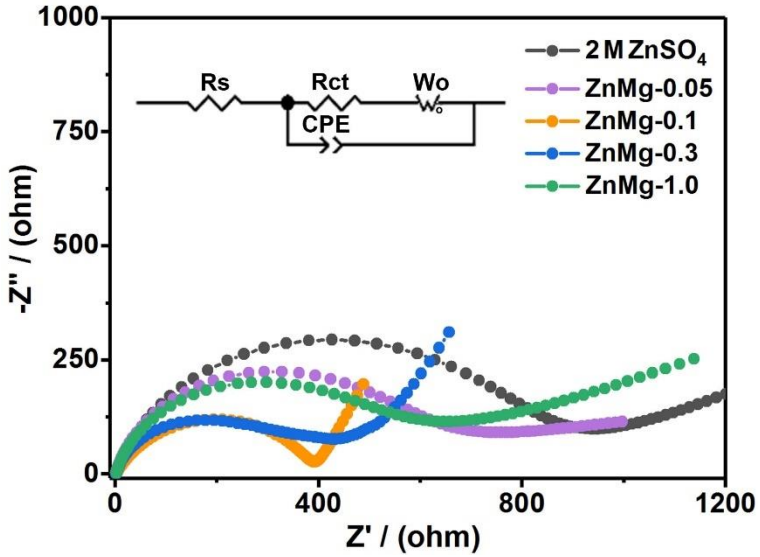

Figure S4. EIS results of ZHCs in different electrolytes.

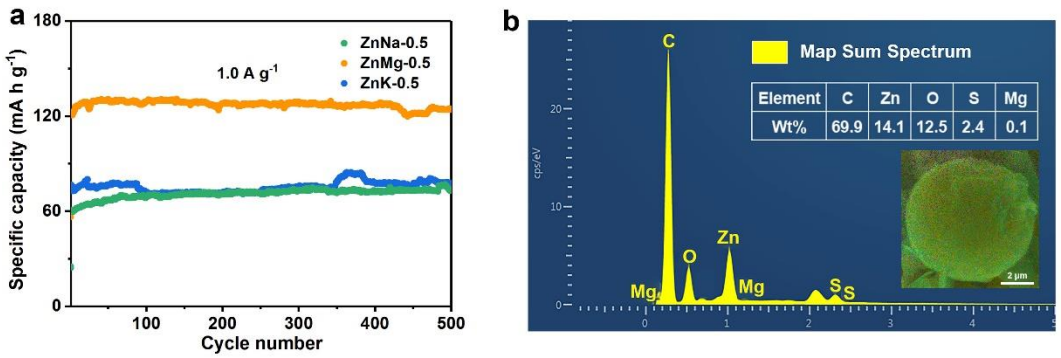

Figure S5. a) Comparison of the cycling performance of AC//2 M $ZnSO_4$//Zn capacitors at 1.0 A g^{-1} with different sulphate additives in the electrolyte. b) Map Sum Spectrum of AC cathode in the fully discharged state with ZnMg-0.1 electrolyte.

The cycling performance of AC//2 M $ZnSO_4$//Zn capacitors with different sulphate additives (0.5 M Na_2SO_4, 0.5 M $MgSO_4$ and 0.5 M K_2SO_4) in the electrolyte at a current density of 1.0 A g^{-1} were compared in **Figure S5a**. The capacitor in ZnMg-0.5 delivers the highest capacity of 125 mA h g^{-1} and others with ZnNa-0.5 and ZnK-0.5 show a lower capacity of about 60 mA h g^{-1}. Since the concentration of sulfate is the same (2.5 M SO_4^{2-}), this capacity difference can be ascribed to the adsorption of cations. Map Sum Spectrum shows the existence of Mg and proves that the adsorption of Mg^{2+} on AC cathode during the discharge process (**Figure S5b**). These phenomena indicate that reversible ions adsorption/desorption on AC cathode provide double-layer capacitance.

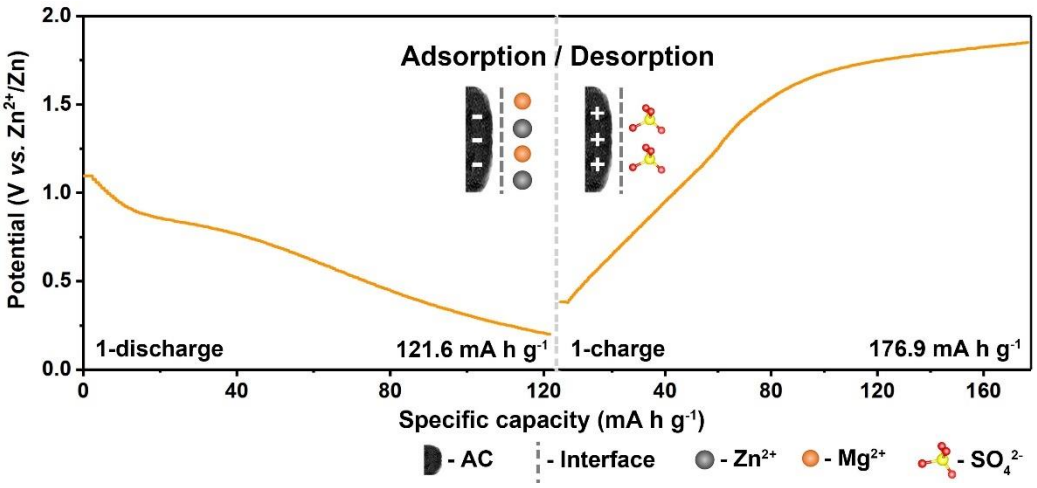

Figure S6. GCD covers of ZHCs in ZnMg-0.1 electrolyte during first cycle at the current density of 1.0 A g^{-1}.

The ZHCs in ZnMg-0.1 electrolyte achieve a high discharge specific capacity of 121.6 mA h g^{-1} in the first discharge state, which proves that the capacity is contributed by the adsorption of metal ions on AC cathode. Due to the low initial voltage (1.095 V) of ZHCs, the capacity is lower than average capacity (about 150 mA h g^{-1}). And the charge specific capacity of 176.9 mA h g^{-1} is achieved in the first charge state accompanied with the adsorption of SO_4^{2-}.

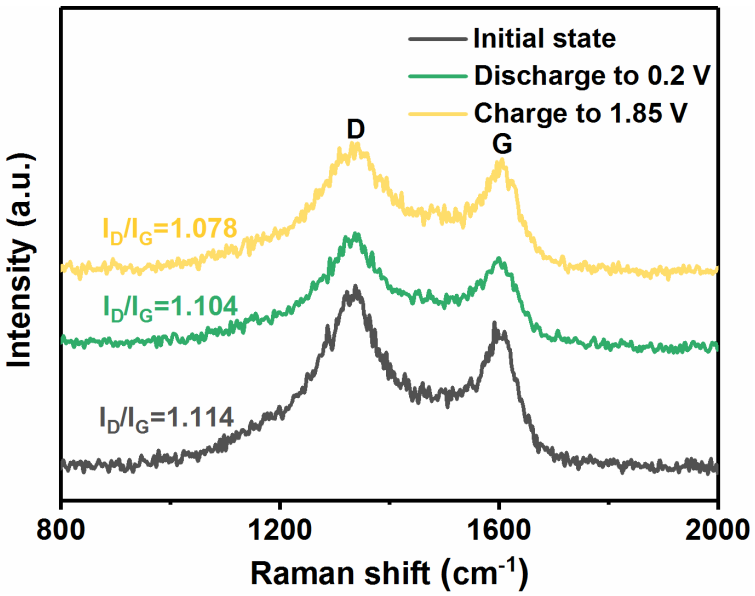

Figure S7. Raman spectroscopy of AC cathodes in the initial, fully discharged and fully charged states in ZnMg-0.1 electrolyte.

The D peak and G peak show periodic changes during the discharge and charge processes. The I_D and I_G ratio of AC at initial state, fully discharged state and fully charged state is 1.114,1.104 and 1.078 in turn, which indicates that the adsorption of Zn^{2+}/Mg^{2+} ions improved defects in structural carbon in the discharging process, and the adsorption of sulfate ions has the same effect in the charging process.[9]

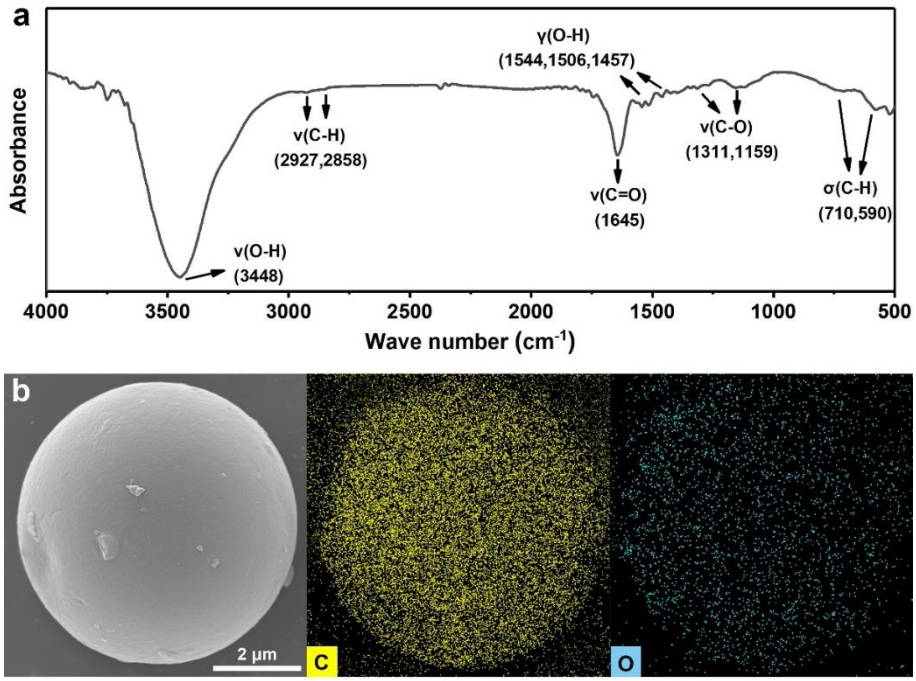

Figure S8. a) FTIR spectra of AC raw materials. b) SEM and EDS mapping images of AC raw materials.

As shown in the FTIR spectra of AC, the characteristic peaks at 2927 and 2858 cm^{-1} are normally recognized as the asymmetric stretching and the symmetric stretching of CH_2, respectively. The board peak at 3448 cm^{-1} is mainly attributable to the stretching vibrations of –OH groups on the active carbon surface. Correspondingly, there are three absorption peaks at 1544, 1506 and 1457 cm^{-1}, which is caused by the bending vibration of hydroxyl groups. Besides, the absorption peak occurring near 1645 cm^{-1} in the medium frequency area is caused by the stretching vibration of C=O. Finally, the absorption peaks at 1311 and 1159 cm^{-1} arise from the vibration of C–O of carboxylic acid and the stretching vibration of C–OH, respectively, which further confirm the introduction of oxygen functionalities onto the surface of AC.[10] The EDS mapping confirms the element of oxygen on the surface of AC raw materials.

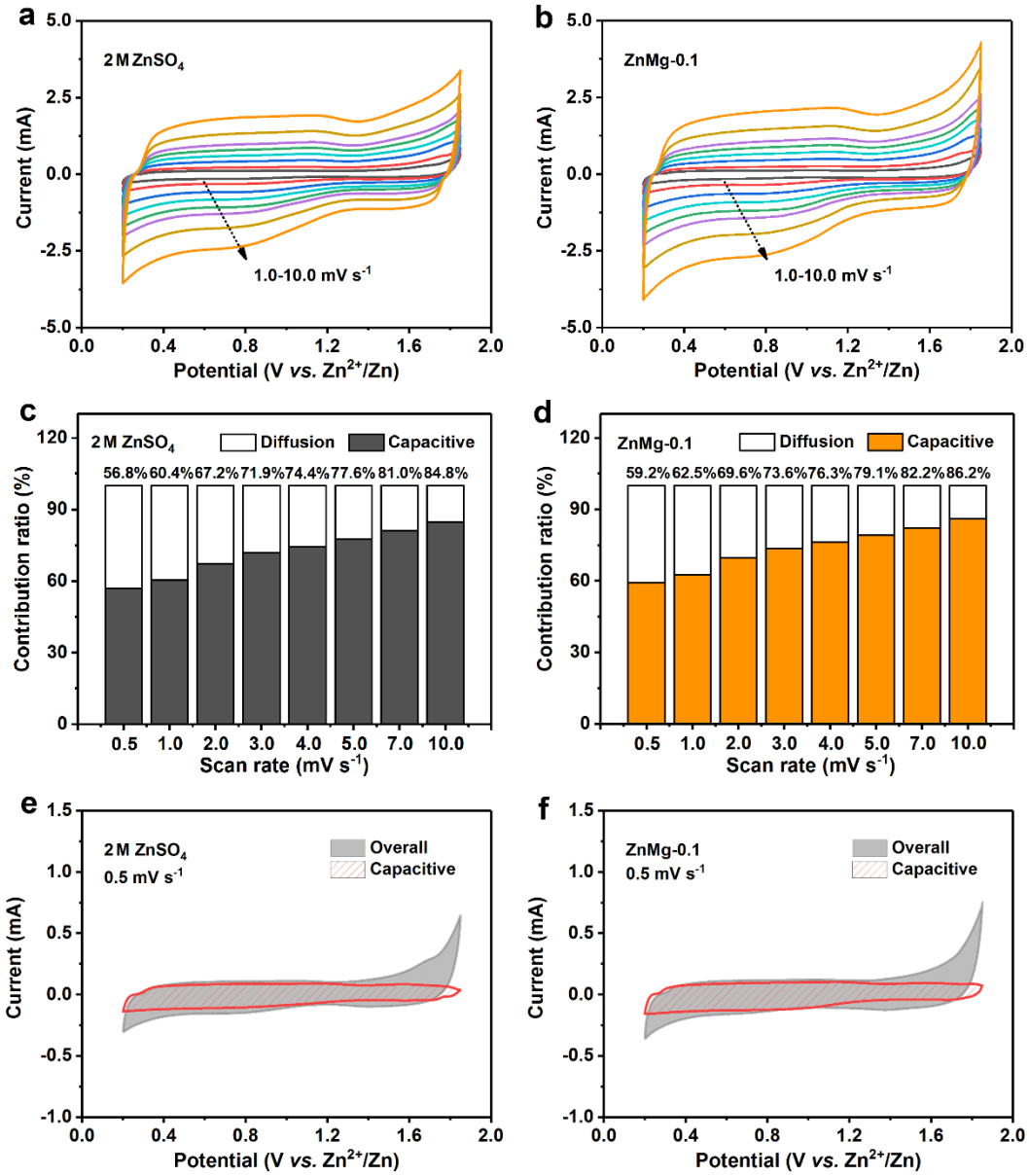

Figure S9. a, b) CV curves at various scan rates of 1.0–10.0 mV s^{-1} in 2 M $ZnSO_4$ (a), in ZnMg-0.1 (b). c, d) The contribution ratios of the capacitive and diffusion-controlled contribution ratios of AC cathode in 2 M $ZnSO_4$ (c), in ZnMg-0.1 (d). e, f) The capacitive contribution calculated at a scan rate of 0.5 mV s^{-1} in 2 M $ZnSO_4$ (e), in ZnMg-0.1 (f).

The CV curves at different scan rates in both electrolytes show similar behavior with the oxidation/reduction wide peaks, which is attributed to the unique surface redox pseudocapacitance mechanism, consistent with the previous work. The reformulation of Equation is further applied to analyze the capacitive and diffusion-controlled contributions to the total capacity of AC electrode:

$$i = k_1 v + k_2 v^{1/2}$$

or describe as

$$\frac{i}{v^{\frac{1}{2}}} = k_1 v^{1/2} + k_2$$

in which, $k_1 v$ and $k_2 v^{1/2}$ are the capacitive and diffusion-controlled contributions of the electrode reactions, respectively.[11]

The capacitive contribution of AC cathode gradually increases with the incremental scan rate. The capacitive-controlled contribution was calculated to be 59.2% at 0.5 mV s^{-1} to 86.2% at 10 mV s^{-1} (**Figure S9d**, in 2 M $ZnSO_4$ is 56.8% to 84.8%, respectively, **Figure S9c**). The capacitive contribution calculated at a scan rate of 0.5 mV s^{-1} in ZnMg-0.1 is about 88.8 mA h g^{-1} (150 mA h g^{-1} * 59.2% = 88.8 mA h g^{-1}, the capacitive contribution of the adsorption of Zn^{2+} and Mg^{2+}), while capacitive contribution in 2 M $ZnSO_4$ (100 mA h g^{-1} * 56.8% = 56.8 mA h g^{-1}, the capacitive contribution of the adsorption of Zn^{2+}) is calculated in the same way. Herein, the capacitive contribution of the reversible adsorption/desorption of Mg^{2+} is about 32 mA h g^{-1}, which is corresponding to the reversible adsorption of Mg^{2+} in **Figure S3**.

In addition, it can be seen from **Figure S9f** that diffusion-controlled reactions occur at the high and low potential, which indicates that the charge storage mechanisms in these ranges are Faradaic.

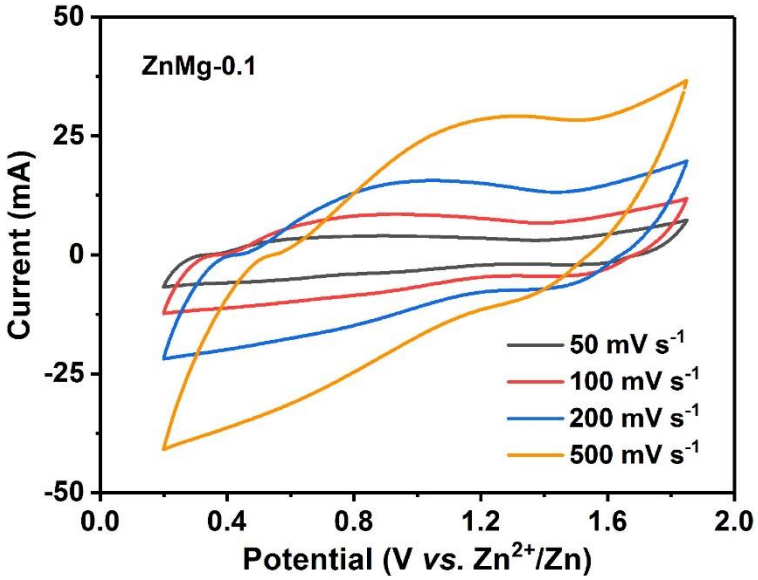

Figure S10. CV curves of AC//ZnMg-0.1//Zn at the scan rate of 50, 100, 200 and 500 mV s^{-1}.

CV curves of ZHCs in ZnMg-0.1 at large scan rates within 0.2–1.85 V are nearly similar, suggesting that the ZHCs can possess rapid electrochemical kinetics and high capacity compared to the pristine electrolyte.

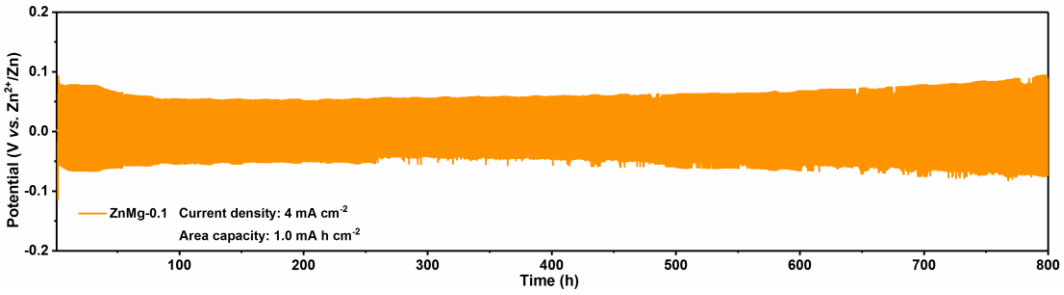

Figure S11. Long-term galvanostatic cycling performance of symmetrical cells in ZnMg-0.1 at a current density of 4.0 mA cm^{-2}.

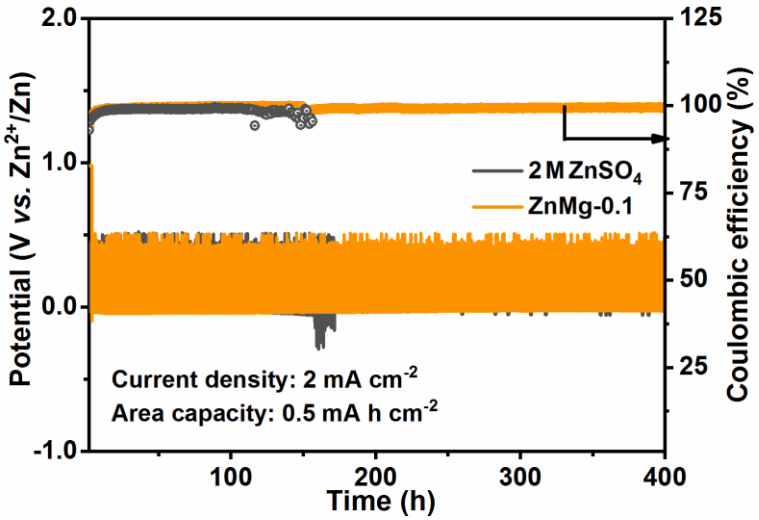

Figure S12. Coulombic efficiency for the long-time performance of Zn versus Cu electrode in 2 M $ZnSO_4$ and ZnMg-0.1 at a current density of 2 mA cm^{-2}.

The cycling performance using Cu as the reference electrode expands to 400 h with about 100 % CE at a current density of 2 mA cm^{-2} in ZnMg-0.1, while the cell in 2 M $ZnSO_4$ exhibits much more fluctuant CE, which positively proved a series of side reactions and irreversibility occurring along with the Zn^{2+} plating/stripping process.

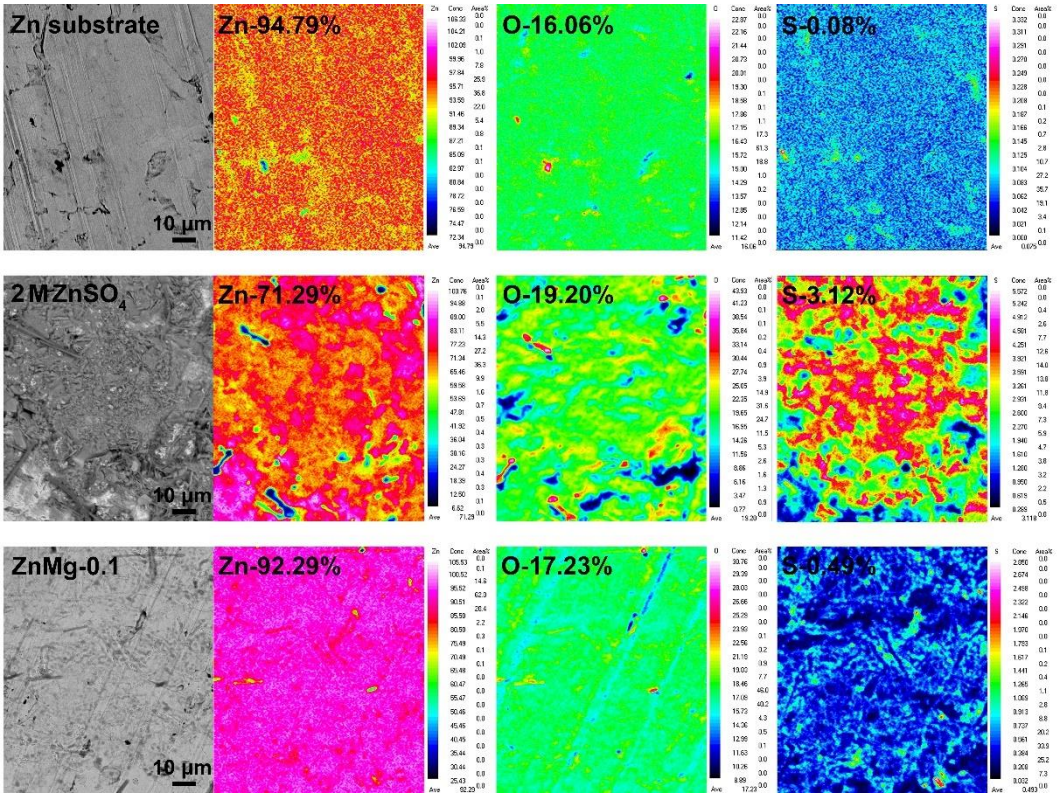

Figure S13. EPMA mapping of Zn substrate and Zn electrodes in 2 M $ZnSO_4$ and ZnMg-0.1 after 20 cycles.

The distribution ratio of Zn, O, and S elements in 2 M $ZnSO_4$ are 71.29%, 19.20% and 3.12%, while in ZnMg-0.1 are 92.29%, 17.23% and 0.49%, which exhibit a little variance to the fresh Zn anode (94.79%, 16.06% and 0.075%).

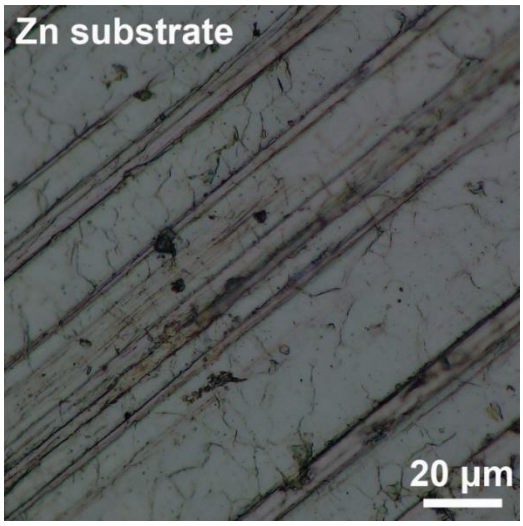

Figure S14. The UTM optical images of Zn substrate.

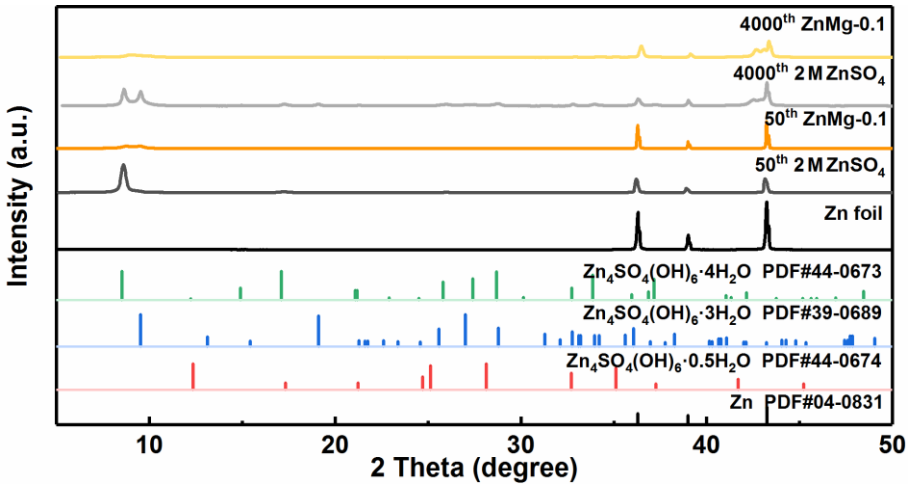

Figure S15. XRD patterns of corresponding Zn anodes after 50 and 4000 cycles.

XRD patterns of corresponding Zn anodes after 50 and 4000 cycles show clean Zn phase without other impurities in ZnMg-0.1 whereas the phases of $Zn_4SO_4(OH)_6{\cdot}xH_2O$ are detected on the surface of Zn in 2 M $ZnSO_4$.

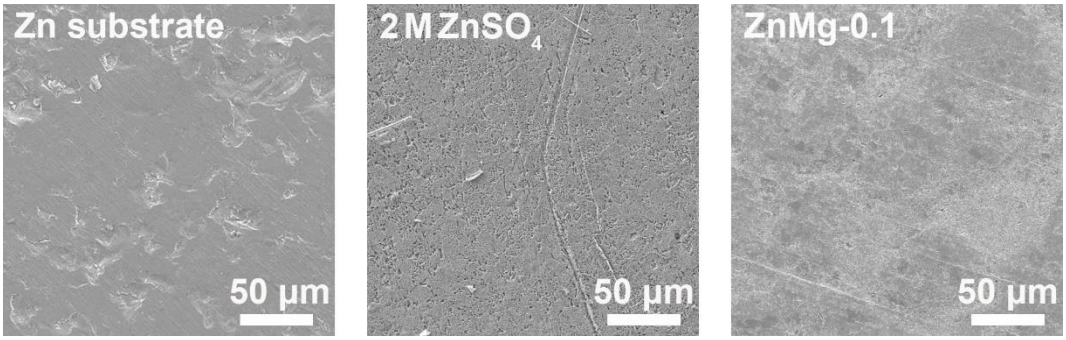

Figure S16. SEM images of Zn electrodes in the initial state and after 20 cycles in 2 M $ZnSO_4$ and ZnMg-0.1 electrolytes.

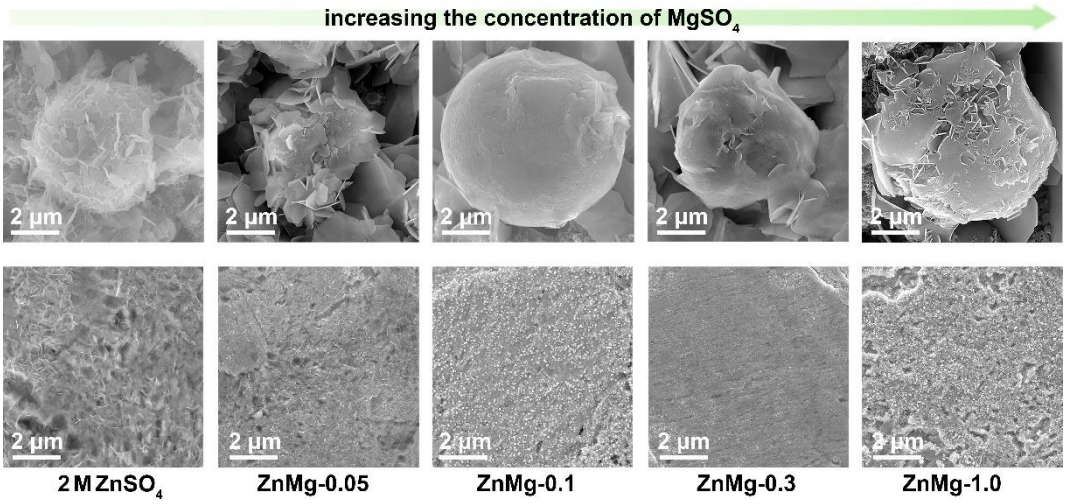

Figure S17. SEM images of AC cathodes discharge to 0.2 V and Zn anodes after 20 cycles with the increasing concentration of $MgSO_4$.

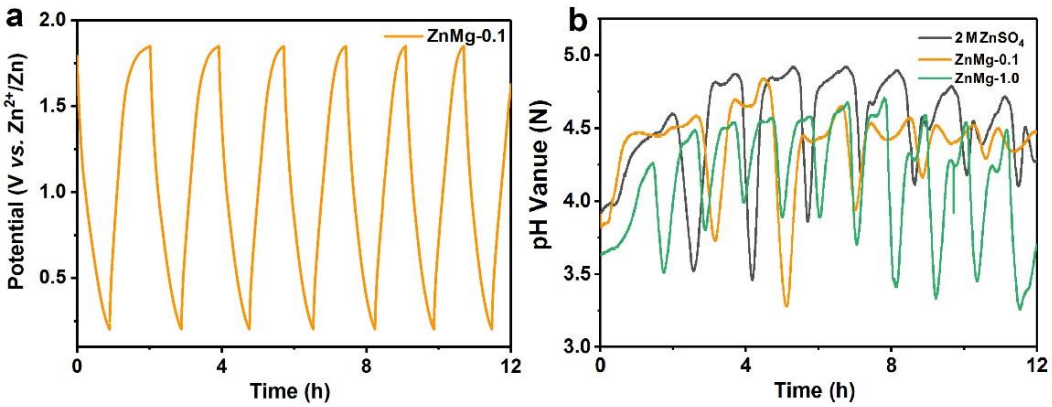

Figure S18. a, b) GCD curve (a) and pH (b) values in different electrolytes during the charge and discharge process at the current of 0.1 A g^{-1}.

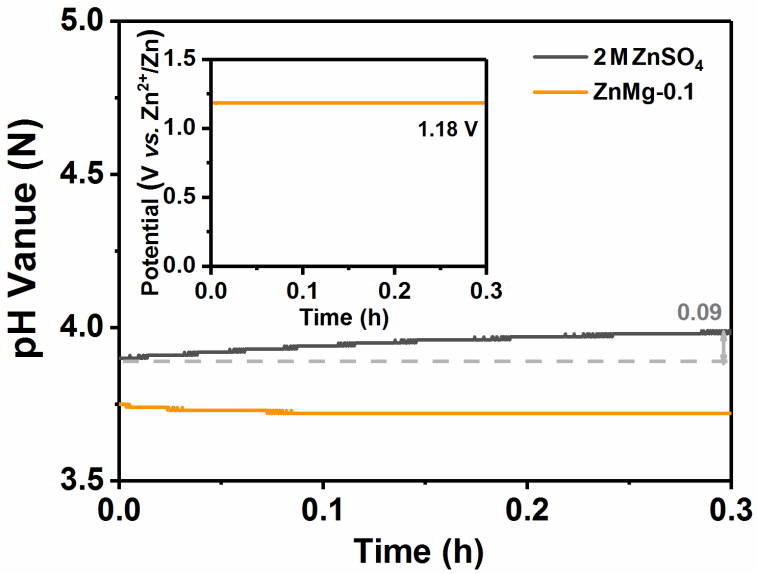

Figure S19. The pH values in different electrolytes at shelving process.

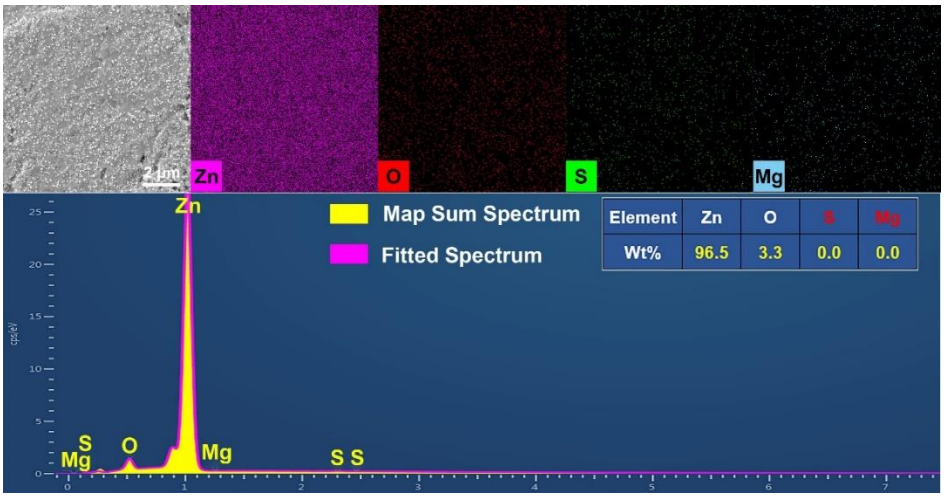

Figure S20. SEM and EDS mapping images of Zn anode in ZnMg-0.1 electrolyte after 20 cycles.

The EDS mapping images clarify that the Mg element is not reduced to the Zn surface during successive cycles, which is in line with the requirements of SHES additives.

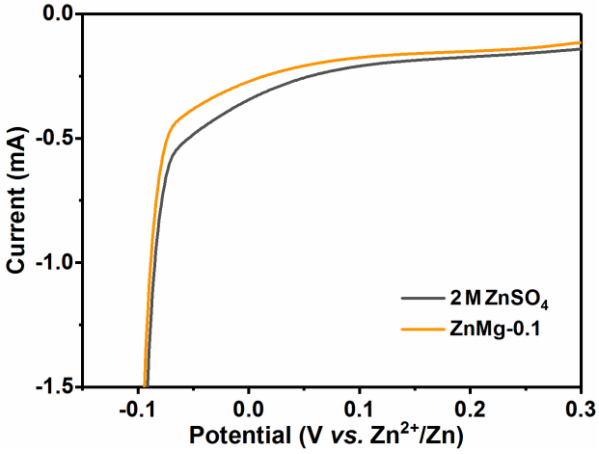

Figure S21. LSV curves of Zn anode in 2 M $ZnSO_4$ and ZnMg-0.1 electrolytes.

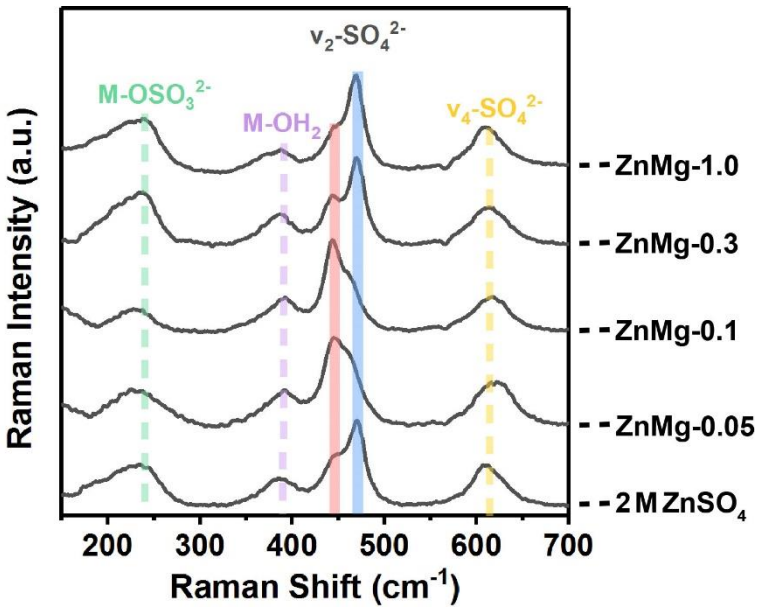

Figure S22. Raman spectroscopy of different concentrations of $MgSO_4$ additive in 2 M $ZnSO_4$.

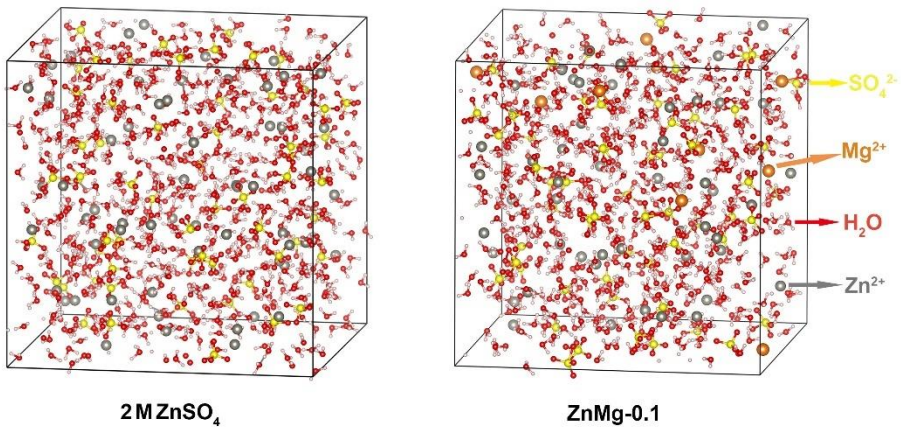

Figure S23. 3D snapshots from MD simulations of 2 M $ZnSO_4$ and ZnMg-0.1 electrolytes.

Supplementary Tables

Table S1. Primary EIS simulation parameters of ZHCs in different electrolytes

Sample	R_s (Ω)	R_{ct} (Ω)
ZnMg-1.0	1.75	653.8
ZnMg-0.3	2.28	392.2
ZnMg-0.1	2.35	380.5
ZnMg-0.05	1.31	680.2
2 M $ZnSO_4$	2.01	919.1

Table S2. Peak value of Raman spectroscopy in different electrolytes

Electrolyte	M-OSO_3^{2-} (a.u.)	M-OH_2 (a.u.)	v_4-SO_4^{2-} (a.u.)
ZnMg-1.0	1477.15	538.23	873.63
ZnMg-0.3	1134.17	606.58	816.57
ZnMg-0.1	358.53	669.93	708.53
ZnMg-0.05	594.74	553.2	858.34
2 M $ZnSO_4$	956.96	690.57	939.69

Table S3. Peak area ratio of Raman spectroscopy in different electrolytes

Electrolyte	v_2-SO_4^{2-} (%)		v-OH_2 (%)	
	SSIP	CIP	HOH-OH_2	HOH-OSO_3^{2-}
ZnMg-1.0	32.65	67.35	69.45	30.54
ZnMg-0.3	40.02	59.98	69.41	30.59
ZnMg-0.1	78.96	21.04	69.19	30.83
ZnMg-0.05	75.30	24.7	73.68	26.32
2 M $ZnSO_4$	53.35	46.65	73.77	26.23

Supplementary Equations

According to the Nernst equation:[12]

$$E_{Red} = E^{\emptyset}_{Red} - \frac{RT}{zF} ln \frac{\alpha_{Red}}{\alpha_{Ox}}$$

where R is the universal gas constant (8.314472 J K^{-1} mol^{-1}), T is the absolute temperature (take T = 298.15 K), and α is the chemical activity for the relevant species (α_{Red} is for the reductant and α_{Ox} for the oxidant). $\alpha_x = \gamma_x c_x$ where γ_x and c_x are the activity coefficient and the concentration of species x. F is the Faraday constant (9.64853399×10^4 C mol^{-1}), and z is the number of moles of electrons transferred. The equation can be simplified as:

$$E_{Red} = E^{\emptyset}_{Red} - \frac{0.05916V}{z} log_{10} \frac{1}{\alpha_{Ox}}$$

In **Figure 4a**, E° is the standard reduction potential (*vs.* SHE) of the cation at 1 M concentration.

References

[1] G. Kresse, J. Furthmuller, *Comp. Mater. Sci.* **1996**, *6*, 15.

[2] G. Kresse, J. Furthmuller, *Phys. Rev. B.* **1996**, *54*, 11169.

[3] J. P. Perdew, K. Burke, M. Ernzerhof, *Phys. Rev. Lett.* **1996**, *77*, 3865.

[4] G. Kresse, D. Joubert, *Phys. Rev. B*. **1999**, *59*, 1758.

[5] P. E. Blöchl, *Phys. Rev. B*. **1994**, *50*, 17953.

[6] P. E. Blöchl, O. Jepsen, O. K. Andersen, *Phys. Rev. B*. **1994**, *49*, 16223.

[7] S.-D. Han, O. Borodin, D. M. Seo, Z.-B. Zhou, W. A. Henderson, *J. Electrochem. Soc*. **2014**, *161*, A2042.

[8] K. B. J. P. Perdew, M. Ernzerhof, *Phys. Rev. Lett.* **1998**, *80*, 891.

[9] Y. Jin, H. Ao, K. Qi, X. Zhang, M. Liu, T. Zhou, S. Wang, G. Xia, Y. Zhu, *Mater. Today Energy*. **2021**, *19*, 100598.

[10] Y. Tian, R. Amal, D.-W. Wang, *Front. Energy Res*. **2016**, *4*, 34.

[11] J. Yin, W. Zhang, W. Wang, N. A. Alhebshi, N. Salah, H. N. Alshareef, *Adv. Energy Mater*. **2020**, *10*, 2001705.

[12] F. Ding, W. Xu, G. L. Graff, J. Zhang, M. L. Sushko, X. Chen, Y. Shao, M. H. Engelhard, Z. Nie, J. Xiao, X. Liu, P. V. Sushko, J. Liu, J.-G. Zhang, *J. Am. Chem. Soc*. **2013**, *135*, 4450.